**Climate
of the Past**

Modeling Northern Hemisphere ice-sheet distribution during MIS 5 and MIS 7 glacial inceptions

F. Colleoni[1]**, S. Masina**[1,2]**, A. Cherchi**[1,2]**, A. Navarra**[1,2]**, C. Ritz**[3]**, V. Peyaud**[3]**, and B. Otto-Bliesner**[4]

[1]Centro Euro-Mediterraneo sui Cambiamenti Climatici, Bologna, Italy
[2]Istituto Nazionale di Geofisica e di Vulcanologia, Bologna, Italy
[3]CNRS/Université Joseph Fourier, Grenoble 1, LGGE, St Martin d'Hères cedex, France
[4]Climate and Global Dynamics Division, National Center for Atmospheric Research, Boulder, CO, USA

*Correspondence to:* F. Colleoni (flocolleoni@gmail.com)

Abstract. The present manuscript compares Marine Isotope Stage 5 (MIS 5, 125–115 kyr BP) and MIS 7 (236–229 kyr BP) with the aim to investigate the origin of the difference in ice-sheet growth over the Northern Hemisphere high latitudes between these last two inceptions. Our approach combines a low resolution coupled atmosphere–ocean–sea-ice general circulation model and a 3-D thermomechanical ice-sheet model to simulate the state of the ice sheets associated with the inception climate states of MIS 5 and MIS 7. Our results show that external forcing (orbitals and GHG) and sea-ice albedo feedbacks are the main factors responsible for the difference in the land-ice initial state between MIS 5 and MIS 7 and that our cold climate model bias impacts more during a cold inception, such as MIS 7, than during a warm inception, such as MIS 5. In addition, if proper ice-elevation and albedo feedbacks are not taken into consideration, the evolution towards glacial inception is hardly simulated, especially for MIS 7. Finally, results highlight that while simulated ice volumes for MIS 5 glacial inception almost fit with paleo-reconstructions, the lack of precipitation over high latitudes, identified as a bias of our climate model, does not allow for a proper simulation of MIS 7 glacial inception.

1 Introduction

Glacial inceptions represent a transition from a warm to a cold mean climate state (Calov et al., 2005b). Indeed, considering the sea-level records during these warm-to-cold transitions, Northern Hemisphere ice sheets were only little developed over North America and Eurasia compared to the glacial maxima (Fig. 1d). Concerns about the capability of climate models to properly simulate future climates have emerged from the large uncertainties and lack of flexibility of the same models to simulate past climate transitions from warm to cold conditions (Calov et al., 2005b). Therefore, glacial inceptions are an interesting phenomenon with which to test the capability of models to simulate climates slightly warmer or slightly colder than present-day climate.

It is now accepted that Northern Hemisphere ice sheets started to develop only if both insolation and greenhouse gases (GHGs) dropped significantly (e.g., Berger, 1978; Bonelli et al., 2009). The amplitude of the drop in insolation and GHGs, however, differs between each glacial inceptions. During the last two glacial inceptions, namely MIS 5 ($\approx$ 125–115 kyr BP) and MIS 7 ($\approx$ 236–229 kyr BP), the concentration of atmospheric CO_2 retrieved from East Antarctica (Luthi et al., 2008) peaked to a rather similar value, but dropped by a larger amount during MIS 7 glacial inception (Fig. 1f). After $\approx$ 242 kyr BP, CO_2 dropped well below 260 ppm, while after 125 kyr BP, CO_2 remained above 260 ppm until $\approx$ 110 kyr BP. Similarly, the largest drop in atmospheric CH_4 concentration occurs after 242 kyr BP (Fig. 1e, Loulergue et al., 2008). Similarities with GHGs trends are also observed in the East Antarctica mean annual temperature anomaly record (Fig. 1g, Jouzel et al., 2007). On the contrary, the largest drop in Northern Hemisphere high latitudes summer insolation is observed after the last interglacial, $\approx$ 125 kyr BP (Fig. 1b).
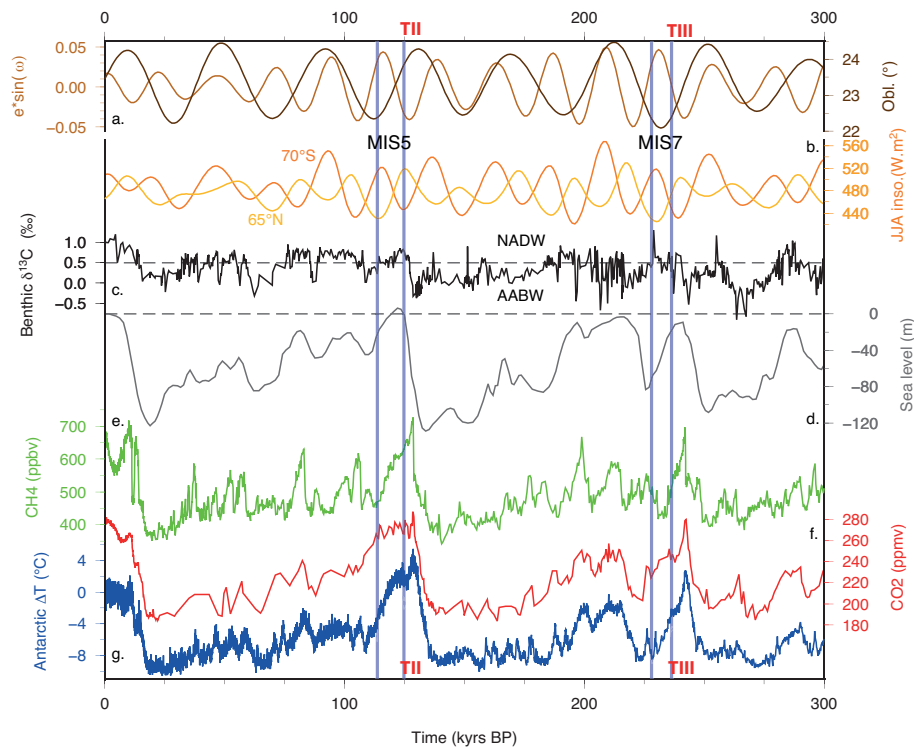
Fig. 1. Overview of the two last glacial cycles illustrated by different forcing and proxies. From top to bottom: **(a)** obliquity (°) and precession index (Laskar et al., 2004); **(b)** summer insolation at 65° N and 70° S (W m^{-2} Laskar et al., 2004); **(c)** benthic δ^{13}C indicative of the changes in sources of the North Atlantic deep waters formation at the Mediterranean latitudes (Martrat et al., 2007); **(d)** sea-level reconstructions (m) from Waelbroeck et al. (2002); **(e)** atmospheric CH$_4$ (ppbv Loulergue et al., 2008) concentrations from EPICA Dome C, East Antarctica; **(f)** CO$_2$ (ppmv Luthi et al., 2008) concentrations from EPICA Dome C, East Antarctica; **(g)** temperature anomaly (°C) relatively to present day (Jouzel et al., 2007), retrieved from deuterium excess, EPICA Dome C, East Antarctica. Vertical grey bars indicate the time of the climate snapshots simulations performed in this work. Termination II (TII) and Termination III (TIII) are indicated as well.

An additional remarkable difference between the last two glacial inceptions is the state of the continental ice volume at the beginning of each glacial inception. While the maximum sea-level fall was similar between the last two glacial cycles, the maximum sea-level rise during the last two interglacials varied with estimates above or below present-day sea level (Fig. 1d, Rabineau et al., 2006; Caputo, 2007). In fact, for the last interglacial (≈ 125 kyr BP), proxies indicate a sea-level rise between 4 to 10 m a.m.s.l. (above mean sea level, Stirling et al., 1995; Kopp et al., 2009; McCulloch and Esat, 2000) implying that part of present-day Antarctica and Greenland ice sheets melted out. In contrast, Dutton et al. (2009) suggest that during the penultimate interglacial, ≈ 245 kyr BP, sea level never rose above present-day mean sea level.

Because of those GHGs particularities (low values during MIS 7) and of the difference in sea level between MIS 5 and MIS 7, we focus our investigations on the Northern Hemisphere ice-sheet distribution of MIS 5 (≈ 125–116 kyr BP) and MIS 7 (≈ 236–229 kyr BP) glacial inceptions. More specifically we investigate the impact of orbital parameters and GHGs on the growth of ice sheets in the Northern

Hemisphere high latitudes. We use an earth system model (in its fully coupled AOGCM version) with appropriate GHGs and orbital forcing to simulate the climate of the inceptions under investigation. The climate simulated by the coupled model is then used to force off-line a 3-D thermo-mechanical ice-sheet model.

Numerous studies have tackled the glacial inception issue using different modeling methods: atmospheric general circulation models (AGCM, e.g., Rind et al., 1989; Dong and Valdes, 1995; Vettoretti and Peltier, 2003); coupled atmosphere–ocean GCMs (AOGCM, e.g., Khodri et al., 2001; Yoshimori et al., 2002); earth system models of intermediate complexity (EMIC, e.g., Meissner et al., 2003); asynchronous coupling between three-dimensional ice-sheet model (ISM) and AGCM (e.g., Peyaud et al., 2007; Herrington and Poulsen, 2012) or AOGCM (e.g., Born et al., 2010); three-dimensional ISM coupled to EMIC (e.g., Calov and Marsiat, 1998; Bonelli et al., 2009; Ganopolski et al., 2010; Ganopolski and Calov, 2012); coupled three-dimensional ISM to AOGCM (e.g., Gregory et al., 2012). The majority of paleoclimate modeling studies have focused on the last glacial inception (≈ 115 kyr BP) and have

simulated a sea-level drop by estimating the amount of perennial snow accumulated over the Northern Hemisphere high latitudes using steady-state experiments (e.g., Vettoretti and Peltier, 2003; Jochum et al., 2011) or transient experiments (e.g., Wang and Mysak, 2002). In these studies the models used were able to broadly simulate perennial snow and ice-sheet growth in the Northern Hemisphere high latitudes where geological evidence is indicative of glacial inception areas. Other studies have performed idealized experiments to determine the thresholds of various regional feedbacks in the climate system that could have triggered a glacial inception in the Northern Hemisphere high latitudes (e.g., Calov et al., 2005a, b). Some of the modeling studies have shown the importance of vegetation and dust in amplifying or inhibiting the growth of the ice sheets during the last two glacial cycles (e.g., de Noblet et al., 1996; Vettoretti and Peltier, 2004; Kageyama et al., 2004; Calov et al., 2005a; Krinner et al., 2006; Colleoni et al., 2009b, a). For example, Kubatzki et al. (2006), using a fully coupled climate–ice-sheet EMIC, showed that during the last glacial inception (≈ 113 kyr BP in their study) the growth of the Laurentide ice sheet could have been delayed by modulating the state of ocean and vegetation. In the same line, Born et al. (2010) suggest that, during the last glacial inception (≈ 115 kyr BP), the growth of the Eurasian ice sheet was delayed by a persistent high oceanic heat transport towards the Northern Hemisphere high-latitude regions.

The present work differs from the previous studies aforementioned for two reasons. The first deals with the treatment of the marine margins in the ISM. In the recent work of Herrington and Poulsen (2012) about the last glacial inception (≈ 115 kyr BP) over North America, no explicit ice shelves are simulated, but their ISM allows for floating ice over areas where ocean depth does not exceed 750 m. The limitation of this method resides in the fact that it may partly limit the growth of ice over oceanic regions deeper than 750 meters and as a consequence may induce incorrect ice distribution and volume. It is worth noting that in our ISM, ice shelves are explicitly simulated but a melting rate of 2.45 m yr^{-1} is prescribed below the shelves for ocean depths larger than 450 m. Born et al. (2010) focused on the entire Northern Hemisphere but no ice shelf dynamics was considered. They argued that given the low ice volume observed during the last inception, the treatment of the marine part was of minor importance. Contrary to these this study, Peyaud et al. (2007) showed that the floating part of the Eurasian ice sheet was essential to its rapid multiple advances and retreats during the last glacial cycle. Even if at the time of the last glacial inception, ice volume was low over both North America and Eurasia, this might not have been the case during MIS 7 glacial inception. For this reason, in the present study, we account for ice shelf dynamics in our ISM simulations.

The second reason deals with the initial conditions in the ISM. Most of past studies have modeled climate and ice sheets of the last glacial inception towards 115 kyr BP,

or for the entire last glacial cycle but discarding the peak interglacial of MIS 5. At that time, Eurasia and North America were ice free and the amount of ice that survived over Greenland is still uncertain. This is why most of the past modeling studies choose to initialize MIS 5 climate either with present-day ice cover or with no ice over Greenland. Contrary to MIS 5, MIS 7 recorded a sea level lower than present day. This implies that some continental ice may have survived from the previous glacial cycle over Eurasia and North America or that the Greenland ice sheet was larger than today, or both. Therefore, we choose to spin up the initial ISM topography to simulated pre-inception climates (i.e., with orbital configuration not favorable to glaciation) in order to obtain an initial Northern Hemisphere ice-sheet topography more in agreement with the time periods considered in our work. Nonetheless, the aim of this study is not to reconstruct a realistic ice evolution over the Northern Hemisphere, but to investigate the main differences resulting from different external forcing. Therefore, the evolution of Greenland in our study is only indicative.

The manuscript is structured as follows: Sect. 2 describes the coupled model, the ice-sheet model, the experimental setup as well as the forcing method used for the ISM simulations; Sect. 3 shows the results from the climate and the ISM models simulations; Sect. 4 discusses the main results in terms of hypothesis at the base of the work. Section 5 summarizes the main conclusions.

2 Methods

We force a 3-D thermo-mechanical ice-sheet model off-line with climate states obtained from atmosphere–ocean coupled simulations. To account for the time evolution of the feedbacks that we want to investigate, we modulate the climate forcing in our ISM experiments by means of a temperature index retrieved from Greenland ice cores. This method has been already used in several studies focusing on specific time slices of the last glacial cycle and has provided realistic results of the ice-sheet evolution over North America and Eurasia (Peyaud et al., 2007; Charbit et al., 2007), over Greenland (Letréguilly et al., 1991; Greve, 2005; Quiquet et al., 2013) and over the Tibetan Plateau (Kirchner et al., 2011).

2.1 Community Earth System Model (CESM)

To simulate past climates, we use the CESM 1.0, which consists of a fully coupled atmosphere–ocean–sea-ice–land model (Gent et al., 2011). The atmospheric component (CAM) has 26 vertical levels and an horizontal resolution of $3.75° \times 3.75°$ (T31) shared with the land component (CLM). The ocean component (POP, displaced pole located over Greenland) has 60 vertical levels and a nominal $3°$ horizontal resolution in common with the sea-ice component (CICE). CESM 1.0 provides the possibility of computing dynamical

Table 1. Climate experiments settings. Greenhouse gas concentrations were retrieved from EPICA Dome C, East Antarctica and come from Luthi et al. (2008) for the CO_2, Loulergue et al. (2008) for the CH_4 and Schilt et al. (2010) for the NO_2 records. The orbital parameters for the pre-industrial control experiment (CTR1850) were set to 1990 while the greenhouse gas were set at their pre-industrial values. For K115 and K229 experiments, the runs were initialized at the 400th model year of the K125 and K236 experiments, respectively.

ID	Epoch	Perihelion date	Obliquity (°)	CO_2 (ppm)	CH_4 (ppb)	NO_2 (ppb)	Spin-up	Length (model years)
CTR0K	1990	4 Jan	23.44	367	1760	316	Present day	400
CTR1850	1990	4 Jan	23.44	284	791	275	Pre-ind.	700
K115	115 kyr BP	14 Jan	22.44	262	472	251	K125 branch	300
K125	125 kyr BP	23 Jul	23.86	276	640	263	125 k	700
K229	229 kyr BP	3 Feb	22.22	224	493	256	K236 branch	300
K236	236 kyr BP	2 Oct	22.34	241	481	267	236 k	700

vegetation and dynamical aeolian dust distribution, but we turned off those options, prescribing the pre-industrial vegetation cover and dust distribution over continents in all our experiments since in this work we want to focus on the impact of external forcing.

CESM experiments setup

The two glacial inceptions under investigation have been selected using the values of the proxy records displayed in Fig. 1. The four snapshots referring to the inception periods are identified by the vertical blue boxes. For the last glacial cycle, the timing of inception is commonly defined in literature between 116–113 kyr BP. In this study, we set up the inception simulations with 115 kyr BP orbital and GHGs values. Determining the timing of the penultimate inception was harder, as observed on the sea-level records (Fig. 1d), since the penultimate glacial cycle does not exhibit a regular decreasing trend in sea level as for the last glacial cycle. This period is characterized by three sea-level high-stands (even if below present-day sea level), the first one occurring right after Termination III towards ≈ 231 kyr BP, the second one occurring towards ≈ 206 kyr BP and the last one occurring toward ≈ 189 kyr BP (Dutton et al., 2009). Considering the sea-level evolution, the penultimate inception occurred after 189 kyr BP. On the other hand, considering GHGs and Antarctica temperature anomaly, the largest peaks occurred right after Termination III, setting the beginning of a new cycle towards 240 kyr BP (Fig. 1e and f). Taking the peak GHGs as a reference state for the beginning of the new cycle, we selected the penultimate inception period using the epoch of the nearest orbital state presenting characteristics similar with the inception at 115 kyr BP. The simulation was consequently set up with 229 kyr BP orbitals and GHGs values. Masson-Delmotte et al. (2010) show that in East Antarctica ice core records, the climate evolution before those two glacial inceptions was highly different. In their work, the last interglacial (≈ 130 kyr BP) appears to be the warmest of the last 800 kyr and was preceded by one of the mildest glacial

periods on record, characterized by a moderate sea-level drop similar to that occurred at the Last Glacial Maximum (LGM). In contrast, the penultimate interglacial (≈ 245 kyr BP) was cool and was preceded by one of the coldest glacial periods on record, characterized by a large drop in sea level. To account for this difference in our ISM experiments, we set up two additional simulations with orbital and GHGs values defined as a compromise between the time of maximum Northern high latitudes summer insolation and the time of the highest sea level preceding each glacial inception (Fig. 1d): one at 125 kyr BP and one at 236 kyr BP.

In summary, six experiments, different in orbital parameters and atmospheric greenhouse gas concentrations, were carried out to explore the discrepancies between MIS 5 and MIS 7 glacial inceptions: a present-day run (CTR0k) accounting for present-day GHGs values, used to show CESM performances; a control run resulting from natural variability only, set to pre-industrial initial conditions (CTR1850) to be compared with our paleo-simulations; two MIS 5 experiments set at 125 kyr BP (K125) and 115 kyr BP (K115) and two MIS 7 experiments set at 236 kyr BP (K236) and 229 kyr BP (K229) (see Table 1). The two inceptions experiments, namely K115 and K229, were branched from K125 and K236, respectively, after 400 years of simulation and were then continued for 700 yr. However, to compare the same model years with the branch experiments, CTR1850, K125 and K236 were also continued to 700 model years. A slight drift still persists in the experiments due to the abyssal circulation (not shown). However, we assume that this drift is small enough to not affect our main conclusions.

2.2 GRenoble Ice Shelf and Land Ice model (GRISLI)

Since the CESM 1.0 does not include a fully coupled ISM, we force the stand-alone GRISLI ISM (Ritz et al., 2001) using the mean climate states computed from our experiments (Table 1). GRISLI is a 3-D thermo-mechanical ice-sheet–ice-stream–ice-shelf model, able to simulate both grounded and floating ice. The grounded part uses the shallow ice

approximation (Hutter, 1983, SIA), whereas ice shelves and ice streams are simulated following the shallow shelf approximation (MacAyeal, 1989, SSA). For more details about the physics, the reader may refer to Rommelaere and Ritz (1996) and Ritz et al. (2001). The ice shelf formulation in GRISLI allows for a more realistic calculation of the ice-sheet growth, and particularly of the advance of ice onto the shallow continental shelves in both hemispheres high latitudes during glaciations. GRISLI is thus particularly adapted for simulating past ice-sheet evolution over time (e.g., Álvarez-Solas et al., 2011; Peyaud et al., 2007).

Ice shelf front positions are determined with a scheme where two thickness criteria must be fulfilled: (1) calving occurs at the ice shelf front when the ice thickness is below 150 m. This value was set up according to Peyaud et al. (2007) and it corresponds to the thickness of most observed ice shelf fronts; (2) for each grid point at the front, the ice coming from the upstream points must fail to maintain a thickness above the threshold. Ice shelves geographical distribution is also controlled by basal melting set according to a depth criterion. Above 450 m depth basal melting is $0.2 \, \text{m} \, \text{yr}^{-1}$ while below this depth basal melting is $2.45 \, \text{m} \, \text{yr}^{-1}$.

The experiments have been designed on a 40 km regular rectangular grid from $\approx 47° \text{N}$ to the North Pole. Non-uniform geothermal heat fluxes are prescribed after Shapiro and Ritzwoller (2004). Since we do not have any precise information about dimensions of the Greenland ice sheet for the periods we are modeling, we initialize our experiments with present-day Greenland ice-sheet topography adapted from ETOPO2 dataset (NOAA, http://www.ngdc.noaa.gov/mgg/global/etopo2.html). We assume that the residual glacio-isostatic response from the LGM ($\approx 21 \, \text{kyr BP}$) is small enough to consider the present-day topography to be in isostatic equilibrium. Greenland ice sheet is spun up to pre-inception climates K125 and K236 (see Sect. 2.2.2).

2.2.1 Temperature index

Reconstructing the time-evolution of past climate to force an ice-sheet model is crucial for the outcomes of the simulations. Previous studies using GRISLI, have realistically simulated the last deglaciation (Charbit et al., 2007), or the Early Weischelian Eurasian ice-sheet growth (Peyaud et al., 2007), or more recently Greenland ice sheet over the last 130 kyr BP (Quiquet, 2012; Quiquet et al., 2013), using indices to modulate climate forcing. Bonelli et al. (2009) performed transient experiments over the entire last glacial cycle using the coupled CLIMBER–GRISLI model (only grounded ice) and modulating some of the simulated variables by means of an index (aeolian dust deposition for example).

To construct our temperature index, we used two different published temperature anomaly reconstructions. The first temperature index ΔT_{GR} is the one reconstructed for Greenland over the last two glacial cycles by Quiquet (2012). This index combines three different types of records: North GRIP $\delta^{18}O$ record (central Greenland, North GRIP members, 2004), North Atlantic ODP 980 sea surface temperatures record (Oppo et al., 2006) and EPICA Dome C, CH_4 record (East Antarctica, Loulergue et al., 2008). The reconstruction is shown in Fig. 3a and the temperature index is expressed as a temperature anomaly relative to pre-industrial time period. For more details about the method see Quiquet et al. (2013). Since ΔT_{GR} corresponds to the evolution of Greenland temperature over time, we assume that this index is consequently broadly representative of the variations in atmospheric temperature over Northern Hemisphere high latitudes in general.
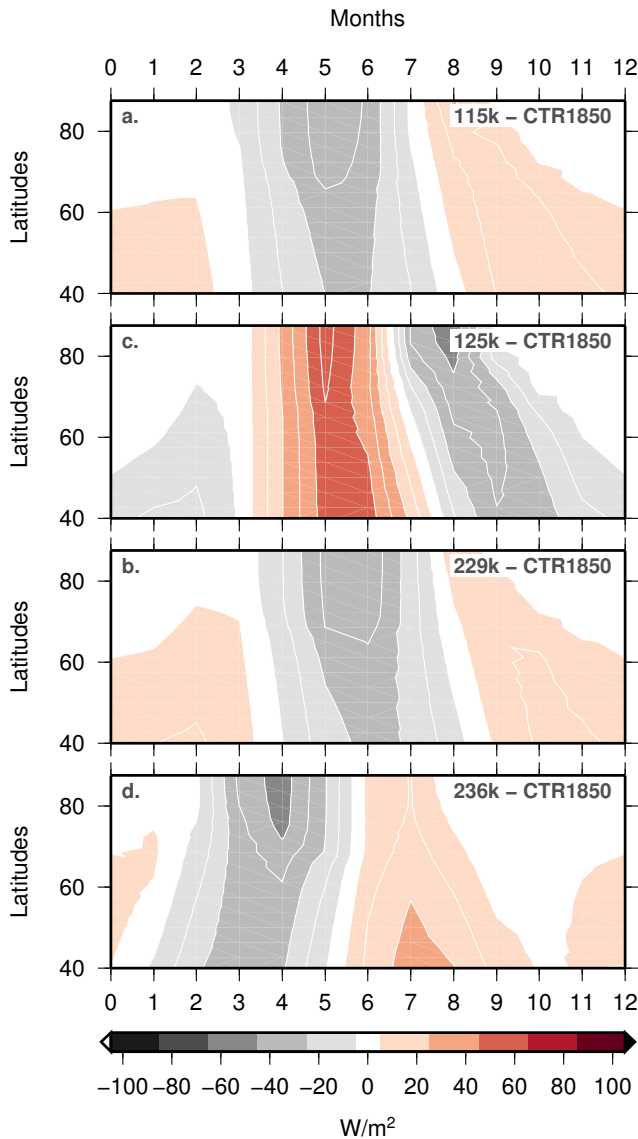
The temperature index ΔT_{GR} is based on various types of observations and results from the feedbacks of the entire earth's climate system. On the contrary, in our climate simulations, we only account for orbitals and GHGs variations. The only simulated ice albedo feedback is due to the sea-ice cover fluctuations. Therefore, the temperature index reconstructed by Quiquet et al. (2013) in its actual shape is not fully consistent with our simulations. To retrieve a time evolution temperature index given by the combination of insolation, GHGs and sea-ice albedo, we considered the reconstructions by Köhler et al. (2010) who used an idealized radiative model applied to various proxy records from Antarctica. Köhler et al. (2010) managed to calculate the mean annual global temperature anomaly, relative to pre-industrial, resulting from the main climate feedbacks acting at paleo-timescale as

$$\Delta T_{\text{tot}}^K = \Delta T_{\text{orbit}}^K + \Delta T_{\text{GHG}}^K + \Delta T_{\text{land cryo}}^K + \Delta T_{\text{sea ice}}^K + \Delta T_{\text{veg}}^K + \Delta T_{\text{dust}}^K, \quad (1)$$

where $\Delta T_{\text{orbit}}^K$, ΔT_{GHG}^K, $\Delta T_{\text{land cryo}}^K$, $\Delta T_{\text{sea ice}}^K$, ΔT_{veg}^K, ΔT_{dust}^K, are the contributions from orbitals, GHGs, land-ice albedo, sea-ice albedo, vegetation and dust, respectively. Köhler et al. (2010) show that ΔT_{tot}^K represents half of the signal from the temperature anomaly retrieved from deuterium excess in East Antarctica (Jouzel et al., 2007). Moreover, the temperature anomaly that they calculated is global, and to apply it to our ice-sheet simulations over the Northern Hemisphere high latitudes, we would need to estimate the time evolution of polar amplification over the high latitudes. Since we cannot calculate it over the time periods considered here, we simply calculated the proportion of total signal (ΔT_{tot}^K) represented by the combination of orbitals ($\Delta T_{\text{orbit}}^K$), GHGs ($\Delta T_{\text{GHG}}^K$) and sea-ice ($\Delta T_{\text{sea ice}}^K$). We finally multiplied Quiquet (2012) temperature index ΔT_{GR} by this ratio:

$$\Delta T_{\text{GIS}} = \Delta T_{\text{GR}} \times \frac{\Delta T_{\text{orbit}}^K + \Delta T_{\text{GHG}}^K + \Delta T_{\text{sea ice}}^K}{\Delta T_{\text{tot}}^K}. \quad (2)$$

The temperature index is displayed for both periods in Fig. 3b and c. For MIS 5, ΔT_{GIS} increases of about 6 °C at 122 kyr BP compared to 125 kyr BP (Fig. 3d) and decrease

Fig. 2. Solar downward radiation anomaly at top of the atmosphere ($W\,m^{-2}$) over the northern high latitudes (40–90° N) between CTR1850 and the experiments described in Table 1.

Table 2. Ice-sheet experiments settings. The experiments are split into two groups: steady state and transient. The steady-states SS229 and SS115 have been branch from SS236 and SS125 respectively. For the transient experiments T115-GIS and T229-GIS, the climate evolution between [236–229 k] and [125–115 k] is perturbed by a temperature index accounting for insolation, greenhouse gas and sea-ice albedo (I_{GIS}) feedbacks from Köhler et al. (2010).
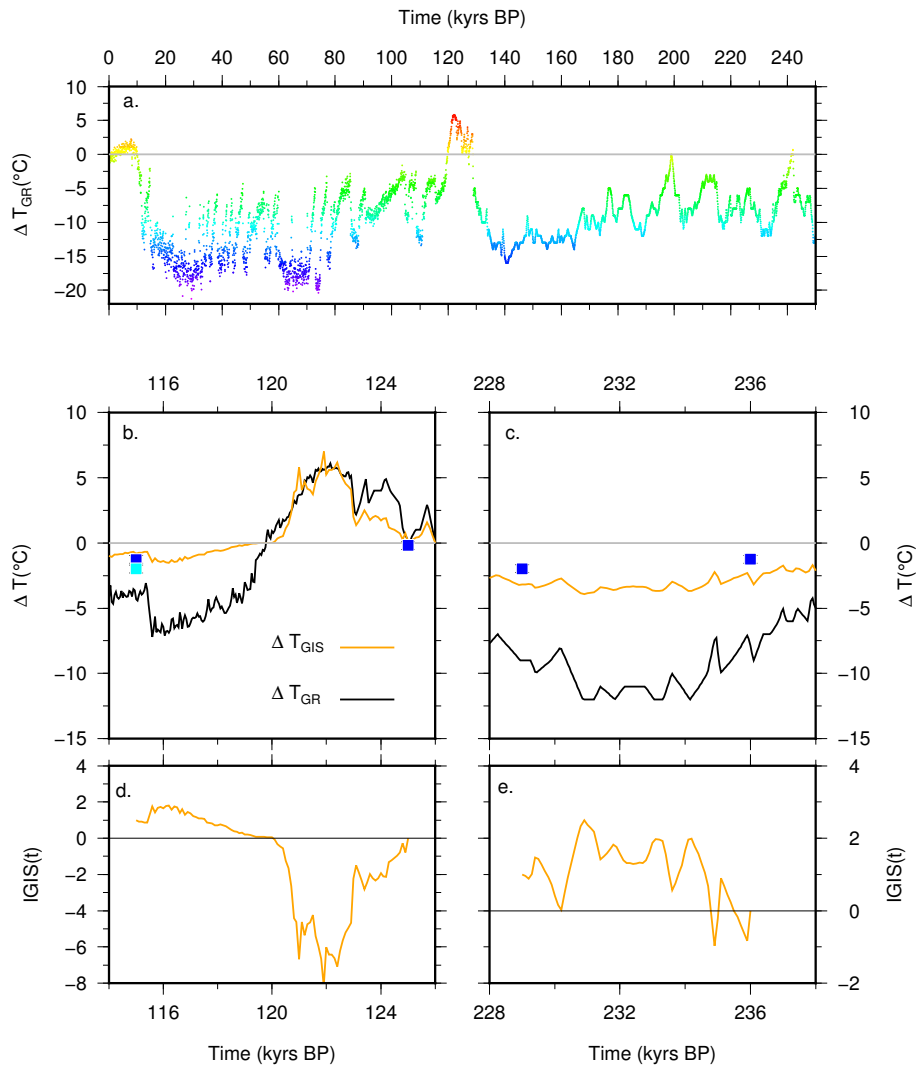
ID	I_{GIS} (°C)	Climate (°C)	Length (kyr)	Spin-up
SS236		K236	0–150	
SS229		K229	150–300	SS236
SS125		K125	0–150	
SS115		K115	150–300	SS125
T229-GIS	X	K236–K229	8	SS236
T115-GIS	X	K125–K115	10	SS125

$I|_{(t)}^{GIS}$ is defined such that $I|_{(t)}^{GIS} = 0$ for the initial time step and denotes interglacial conditions while $I|_{(t)}^{GIS} = 1$ for the final time step denotes more glacial inception conditions (Fig. 3d and e). Therefore, the function is calculated such that $I|_{(t)}^{GIS} < 0$ corresponds to warmer climate conditions while $I|_{(t)}^{GIS} > 0$ corresponds to colder climate conditions. The glacial index function for both periods is displayed in Fig. 3d and e. In the following sections, $I|_{(t)}^{GIS}$ will be referred to as I_{GIS}. Note that with this index, we do not aim at reconstructing the exact conditions during MIS 5 and MIS 7 over the Northern Hemisphere. In fact, I_{GIS} is idealized and probably overestimates the Northern Hemisphere contribution of the feedbacks included in their calculation since original data ΔT_{GIS} is based on central Greenland temperature proxies. Nevertheless, I_{GIS} is indicative of the natural trend of climate evolution in the Northern high latitudes during both time periods.

2.2.2 Ice-sheet experiments setup

Two series of experiments were performed: (1) steady state and (2) transient. To carry out the steady-state experiments, GRISLI was run for 150 000 model years both for 236 kyr BP (SS236) and 125 kyr BP (SS125) time periods using K236 and K125 climate forcing and starting from present-day topography. The steady-state runs for 229 kyr BP (SS229) and 115 kyr BP (SS115) were branched from the last iteration of previous steady-state experiments (SS236 and SS125). They were forced using K115 and K125 climates and ran for a further 150 000 model years (Table 2).

Given the very similar incoming solar radiation pattern at both inception times, i.e., 115 and 229 kyr BP (Fig. 2a and c), simulating the growth of ice sheets by means of steady-state experiments might not highlight the possible differences between those two inceptions. We then decided to perform transient experiments spanning 236–229 and 125–115 kyr BP

of about 7 °C after 122 kyr BP, in agreement with the evolution of the Greenland temperature index from Quiquet et al. (2013) (Fig. 3a and b). For MIS 7, the temperature index is always negative and the maximum temperature decrease is of 2.5 °C relative to 236 kyr BP value (Fig. 3c). For this period, ΔT_{GIS} suggests that the role of combined orbitals, GHGs and sea-ice to the total signal is minor (Fig. 3a and c).

The temperature index is then used to define a glacial index function:

$$I|_{(t)}^{GIS} = \frac{\Delta T|_{(t)}^{GIS} - \Delta T_{125k,236k}^{GIS}}{\Delta T_{115k,229k}^{GIS} - \Delta T_{125k,236k}^{GIS}}. \qquad (3)$$

Fig. 3. Temperature indices considered in this work: **(a)** temperature index ΔT_{GR} (anomaly relative to pre-industrial in °C) after Quiquet (2012). **(b)** and **(c)** ΔT_{GR} (black) as in **(a)** represented by combined contribution of orbitals, GHGs and sea-ice-cover albedo feedbacks (ΔT_{GIS}) retrieved from Köhler et al. (2010). See Methods for more details on the calculations. Dark blue squares correspond to the simulated mean annual central Greenland temperature anomaly (relative to CTR1850) for each of the CESM experiments (Table 1). The light blue square corresponds to the central Greenland temperature anomaly between pre-industrial and 115 kyr BP simulated climates at $1° \times 1°$ horizontal resolution from Jochum et al. (2011). **(d)** and **(e)** glacial index function (Equ. 3) used in the ice-sheet experiments, I_{GIS} including orbitals, GHGs and sea-ice albedo.

where the initial ice topography is that of the steady states for each period, that is, SS236 and SS125, respectively. Since we have available only two simulated climatologies for each inception period, the time evolution of temperature between K236 and K229 and between K125 and K115 is interpolated during the time integrations.

Temperature is corrected for elevation changes, $\Delta T_{topo}|_{(x,y,t)}$, using a spatially uniform lapse rate of $5\,°C\,km^{-1}$ for mean winter temperature (Abe-Ouchi et al., 2007; Bonelli et al., 2009) and $4\,°C\,km^{-1}$ for mean summer temperature (Bonelli et al., 2009). The annual temperature cycle in GRISLI is approximated by a sinusoidal function

based on mean annual and warmest summer month CESM temperatures. Since a simple linear interpolation might not realistically represent the observed time evolution of climate between each simulated climatology (Fig. 1), a time-dependent perturbation is accounted for, following Greve (2005):

$$\Delta T_{S2-S1}^{pert}|_{(x,y,t)} = I|_{(t)}^{GIS} \times \Delta T_{S2-S1}|_{(x,y)} \qquad (4)$$

$$T_{rec}|_{(x,y,t)} = T_{S1}|_{(x,y)} + \Delta T_{S2-S1}^{pert}|_{(x,y,t)} + \Delta T_{topo}|_{(x,y,t)}, \quad (5)$$

where $\Delta T_{S2-S1}|_{(x,y)}$ is the anomaly between our simulated climate snapshots (i.e., K115–K125 and K229–K236), and where $I|_{(t)}^{GIS}$ is defined as in Eq. (3). Calculation of

precipitation field is achieved similarly to temperature, accounting for $I|_{(t)}^{\mathrm{GIS}}$. Note that the use of exponential function in the precipitation formulation is motivated by the saturation pressure of water vapor in the atmosphere which increases roughly exponentially with temperature:

$$P_{\mathrm{rec}}|_{(x,y,t)} = P_{\mathrm{S1}}|_{(x,y)} \times \exp\left[I|_{(t)}^{\mathrm{GIS}} \times \ln\left(\frac{P_{\mathrm{S2}}|_{(x,y)}}{P_{\mathrm{S1}}|_{(x,y)}}\right)\right], \quad (6)$$

where $\frac{P_{\mathrm{S2}}|_{(x,y)}}{P_{\mathrm{S1}}|_{(x,y)}}$ is the ratio between our simulated climate snapshots and calculated as K115/K125 and K229/K236. Precipitation is converted into snowfall when air temperature drops below $2\,^{\circ}\mathrm{C}$. The ablation is calculated using the positive degree day method (PDD, Reeh, 1991) for which the melting coefficients have been set to $C_{\mathrm{snow}} = 3\,\mathrm{mm}\,^{\circ}\mathrm{C}^{-1}\,\mathrm{d}^{-1}$ and $C_{\mathrm{ice}} = 8\,\mathrm{mm}\,^{\circ}\mathrm{C}^{-1}\,\mathrm{d}^{-1}$. Finally, 60 % of surface melt is able to refreeze.

Two sets of transient experiments were performed, namely T115-GIS and T229-GIS based on the temperature index accounting for orbitals, GHGs and sea-ice albedo variations (Table 2).

3 Results

3.1 CESM climate simulations

The orbitals for both inceptions are almost similar since perihelion occurred in mid-January for K115 and at the beginning of February for K229 (Table 1). This leads to a similar solar incoming downward radiation pattern over the Northern Hemisphere high latitudes with colder summers and slightly warmer winters with respect to the pre-industrial control run CTR1850 (Fig. 2). In contrast, pre-inception simulations K125 and K236 differ, with perihelion dates in late July and in early October, respectively (Table 1). This has consequences on permanent snow cover, which is likely to disappear in K125 due to the strong summer insolation.

Compared to CTR1850, mean summer air temperature (JJA) for K125 is warmer by about $3\,^{\circ}\mathrm{C}$ over the Northern Hemisphere high latitudes, while for all the other periods it remains cooler by at least $2\,^{\circ}\mathrm{C}$ (Fig. 4a–d). It is interesting to note that from K125 to K115 the reduction in mean summer temperature is approximately $4\,^{\circ}\mathrm{C}$, while from K236 to K229 the reduction is only about $1\,^{\circ}\mathrm{C}$. The mean annual global cooling due to both inceptions is moderate if compared to CTR1850: on the order of $0.5\,^{\circ}\mathrm{C}$ ($1\,^{\circ}\mathrm{C}$) for the MIS 5 (MIS 7) inception period (Table 3). The contribution of the Northern Hemisphere (0–90° N) to this global cooling ranges from 50 % in K125 to 75 % in K115, while it only differs by about 8 % from K236 to K229 (Table 3). This indicates that inter-hemisphere heat transport is probably larger during MIS 5 than during MIS 7. Moreover, this also suggests that in our MIS 7 experiments and in absence of prescribed Northern Hemisphere ice sheets, Antarctica and its associated sea-ice cover contribute almost as much as the

Table 3. Mean annual air temperature anomaly (°C) for each experiment relative to CTR1850 for global (ΔT_{glob}) and both hemispheres (ΔT_{NH} and ΔT_{SH}). $\Delta T_{\mathrm{NH/glob}}$ corresponds to the ratio (%) between Northern Hemisphere and global mean annual air temperature anomaly relative to CTR1850.

ID	ΔT_{glob} (°C)	ΔT_{NH} (°C)	ΔT_{SH} (°C)	$\Delta T_{\mathrm{NH/glob}}$ (%)
K115	−0.45	−0.68	−0.22	75
K125	−0.43	−0.42	−0.43	50
K229	−0.96	−1.228	−0.70	64
K236	−0.87	−0.97	−0.78	56

Northern Hemisphere snow and sea-ice albedo feedback to the mean annual global cooling, while this is not the case during MIS 5.

The cooling due to the imposed external forcing in K115, K229 and K236 is further strengthened by a substantial thickening of the sea-ice cover and of the accumulation of a perennial snow layer on the top of sea ice (not shown), causing an increase in the local albedo (not shown, e.g., Jackson and Broccoli, 2003). In K115, K229 and K236, sea ice is thicker by about 2 m in the central Arctic Ocean with a concentration of 100 % and by about 1 m along the Canadian and Siberian coasts with a concentration of 85 to 90 %. In K125, differently from the other experiments, sea-ice thickness is reduced by about 2 m in the central Arctic and up to 2.4 m nearby the Bering Strait (not shown). The concentration is 100 % over the entire Arctic ocean, except along the coasts where it ranges between 75 to 85 %. The maximum southward extent of the sea-ice cover (SIC) is fairly similar in all the experiments, with the Norwegian Sea permanently ice free (not shown). Although the sea-ice cover thickens in K115, K229 and K236, the associated increase in local albedo mainly results from the presence of a thick layer of snow accumulated on the top of the sea ice. In fact, in CESM, snow albedo value is set to 90 %, while ice albedo is set to 60 %. In K125, the top snow layer and part of sea ice melted during the summer months. This consequently causes a decrease in the local albedo which contributes to the regional warming (not shown).

The high latitudes cooling simulated in K115, K229 and K236 is mainly responsible for the decrease in precipitation over the Arctic region. Compared to CTR1850, mean annual precipitation over the 30–90 °C latitudinal band is reduced by 11 % in K115, by 13 % in K229 and by 7 % in K236, while in K125 there is no differences with respect to CTR1850 (Fig. 4e–h). Locally, precipitation decreases over the inception areas (Canadian archipelago, northern Norway, Svalbard and the Russian Arctic islands) and over the Bering Strait by about 20 % in K115 and K229 and by about 15 % in K236 relatively to CTR1850. Precipitation is also reduced up to 10 % between Iceland and Svalbard in K125 (Fig. 4f),
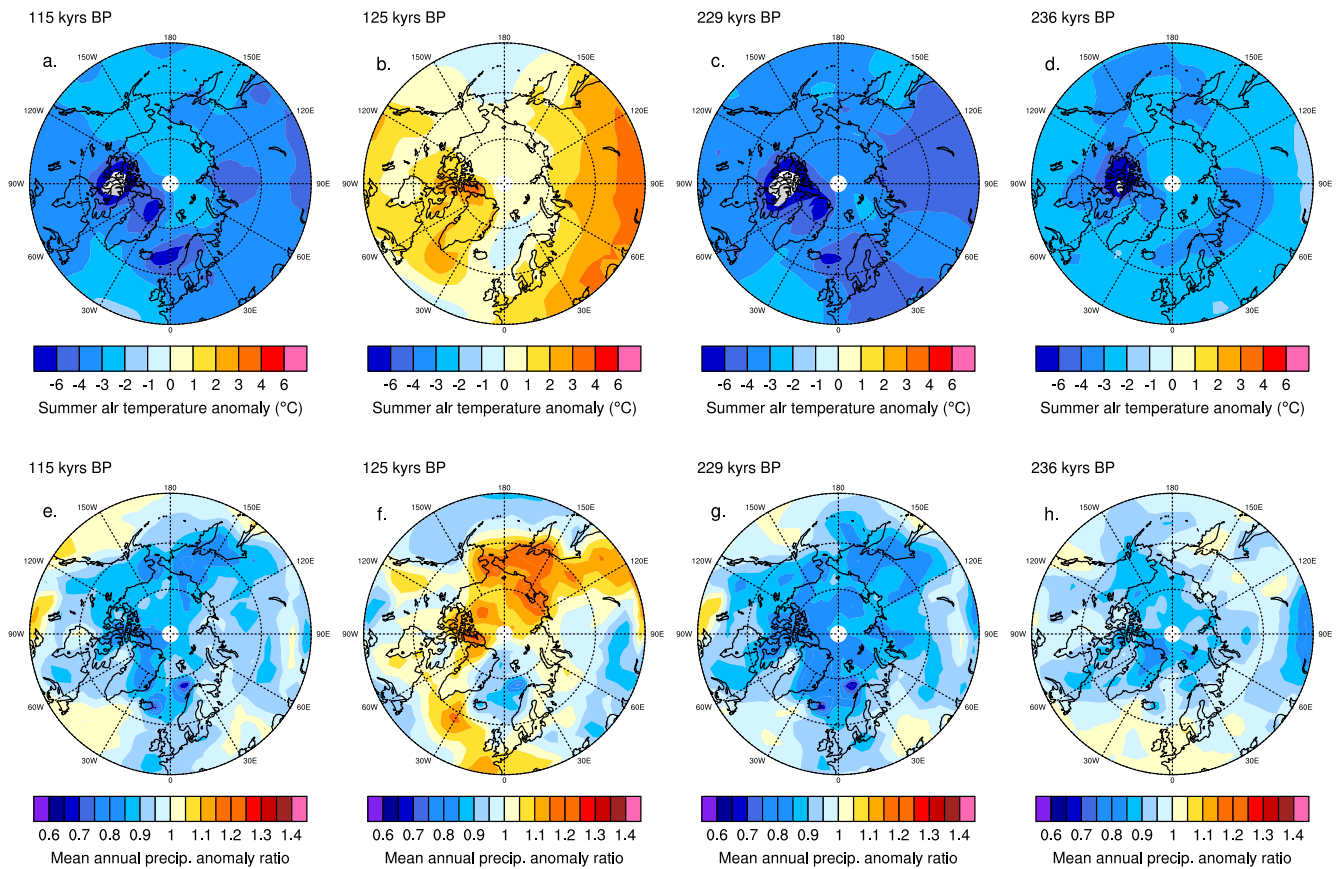
Fig. 4. Simulated air temperatures and precipitation anomalies relatively to pre-industrial control run (CTR1850) in the Northern Hemisphere 45 to 90° N. Top row **(a)**–**(d)** simulated mean summer air temperature anomaly (June-July-August, JJA) in °C calculated as the difference between each experiment and CTR1850. Bottom row **(e)**–**(h)** simulated mean annual precipitation anomaly calculated as the ratio between each experiment and CTR1850 (dimensionless).

because in that simulation sea-ice cover is more extended than in CTR1850 (not shown). As opposed to K115, K229 and K236, and in agreement with temperature increase resulting from the external forcing, precipitation is larger by about 20 % over the inception areas and over the Bering Strait in K125 with respect to CTR1850.

Due to the variations in temperature and precipitation described above, a perennial snow cover develops in all the experiments but its extent varies according to summer temperature and/or precipitation spatial patterns. In K236 and K115, perennial snow is located all along the continental arctic margins, on Svalbard, on the islands of the Barents Sea and Kara Sea and on the Canadian archipelago (Fig. 5b and c). The American Cordilleras are also covered in K115. In contrast, in K125 and K229, the extent of perennial snow is much reduced and is confined exclusively to the eastern part of the Canadian archipelago, Svalbard and the islands of the Barents Sea and Kara Sea (Fig. 5a and d). However, while the extent of perennial snow in K125 is reduced due to the warm summer temperatures, the limited spatial cover in K229 mainly results from a lack of precipitation over the

areas that are covered by perennial snow in K236 (Fig. 4g and h).

The climatic features described above seem to be realistic given the initial conditions (Table 1). However, the low-resolution CESM is affected by some specific biases. The present-day control run CTR0k underestimates temperatures over Northern Eurasia up to 27 °C in winter and by about 3 °C in summer (Fig. 6a and b). This is mainly explained by a weak North Atlantic heat transport towards high latitudes caused by the low spatial resolution (Jochum et al., 2011; Shields et al., 2012). The cold bias over Siberia induces a substantial reduction in precipitation over these regions of at least 90 % during winter and of about 70 % during summer (Fig. 6c and d) if compared to the Global Precipitation Climatology Project precipitation data sets (GPCP, Adler et al., 2003). On the contrary, both temperature and precipitation are overestimated over the western part of North America.

Despite those biases, the simulated mean annual central Greenland temperature anomaly (relative to CTR1850, blue squares in Fig. 3b and c) is in good agreement with the temperature index of central Greenland accounting for orbital,
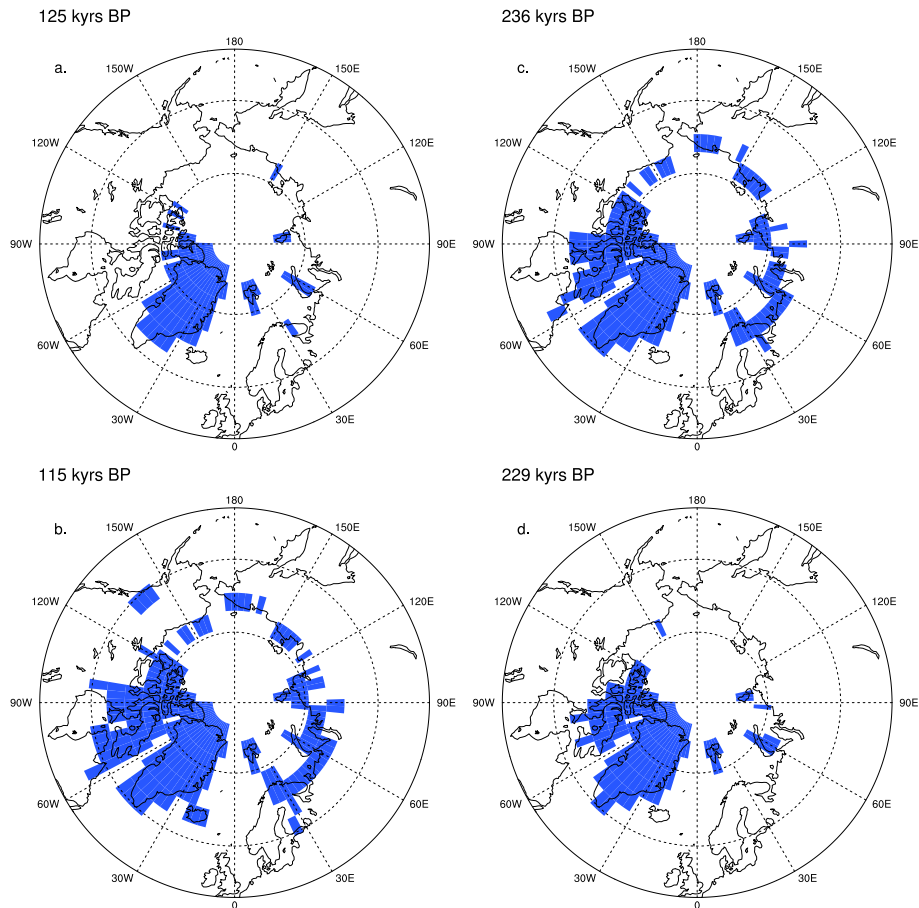
Fig. 5. Simulated perennial continental snow cover for each climate experiment, **(a)** K125, **(b)** K115, **(c)** K236 and **(d)** K229. Snow cover is considered as perennial when residence time is 365 days.

GHGs and SIC albedo feedback (orange curve in Fig. 3b and c). Assuming that the uncertainty on this temperature index is similar to that of our simulated temperatures, this indicates that our two simulations K125 and K115 are able to capture a realistic impact of orbital, GHGs and SIC albedo on temperatures in the Northern Hemisphere. It also suggests that the negative precipitation bias associated with the negative temperature anomaly has a minor impact at that time. However, this might not be the case in K236 and K229 where mean annual temperature anomalies smaller than that of the temperature index. The temperature anomaly is certainly limited by the lack of precipitation inducing a reduction in the snow cover extent in both experiments, which in turn may affect the snow albedo feedback.

3.2 Ice-sheet experiments

In this section we use the simulated air temperature and precipitation previously described to force the GRISLI ISM. In the following the ice volume variations will be expressed in meters sea-level equivalent (m SLE) calculated as

$$\text{SLE} = \frac{\rho_\text{I}}{\rho_\text{W}} \times \frac{\sum\limits_{i=1}^{N} \text{thk}_i \times \Delta x \times \Delta y}{4\pi R^2 \times A_0}, \tag{7}$$

where ρ_I is the ice density ($917\,\text{g cm}^{-3}$), ρ_W is the seawater density ($1018\,\text{g cm}^{-3}$), N is the total number of grid pixels, thk is the simulated total ice thickness, Δx and Δy correspond to the horizontal grid increment ($40\,\text{km}$), R stands for the radius of the earth ($3671\,\text{km}$) and A_0 corresponds to the present-day surface ratio between oceans and continents (≈ 0.72).

3.2.1 Steady-state ice-sheets experiments

The time-evolution of all model spin-ups is similar for SS236, SS229 and SS115: equilibrium is reached after about 100 000 model years. For SS125, spin-up is reached after 120 000 model years because part of Greenland is melting. The ice-sheet distribution for each experiment SS236, SS229, SS125 and SS115 (Fig. 8) is in good agreement with the extent of perennial snow simulated by CESM (Fig. 5). More specifically, the areas where the ice sheets
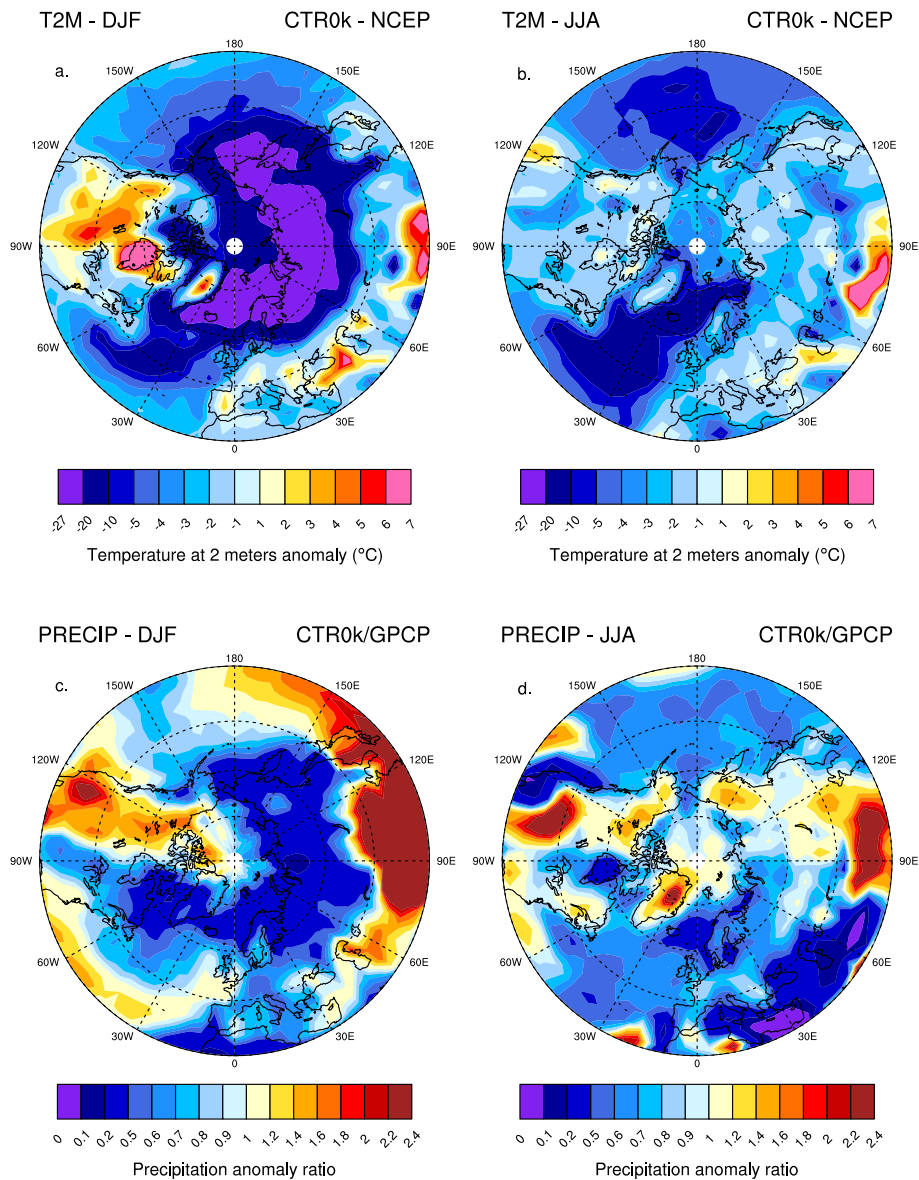
Fig. 6. Bias in temperature and precipitation in the Northern Hemisphere in the low resolution present-day anthropogenic run CTR0k (Table 1) compared to NCEP reanalysis air temperature (Kalnay et al., 1996) and GPCP precipitation data set (Adler et al., 2003). **(a)** and **(b)** simulated winter (DJF) and summer (JJA) air temperature anomaly (°C) between CTR0k and NCEP reanalysis. **(c)** and **(d)** precipitation anomaly ratio (dimensionless) between CTR0k and GPCP precipitation data set.

grow correspond to a residence snow time of 365 days per year. In SS236, SS229 and SS115, the main common inception areas are covered by ice sheets except in the Cascades mountains (Fig. 8b–d). Over this particular region, the CESM underestimates precipitation (Fig. 6), thus limiting the growth of ice in GRISLI. Some mismatch between the perennial snow and the ice-sheet distribution in SS236 and SS115 is visible over eastern Siberia as well. This is because the amount of precipitation in K115 and K236 over this region is too low to permit ice-sheet growth in GRISLI. The evolution of ice distribution from SS236 to SS229 and from SS125 to

SS115 is also in agreement with the evolution of simulated perennial snow from K125 to K115 and from K236 to K229. From SS125 to SS115, the ice sheets expand over North America and Eurasia because of temperature drop in K115 relatively to K125. On the contrary, from SS236 to SS229 both North American and Eurasian ice sheets retreat northward. This is because precipitation strongly decreases from K236 to K229 over the areas where ice sheets grow, which induces a smaller mass balance in SS229 than in SS236.

The total ice volume simulated in the steady-state experiments is in agreement with observations only for SS125 and

SS236 (Fig. 9). In SS125, the simulated final ice volume (i.e., removing about 7.1 m SLE for the present-day Greenland ice sheet) amounts to 1.13 m SLE above present-day mean sea level. In fact, the southernmost part of Greenland melted during the simulation (Fig. 8a). This result is induced by the orbital configuration at 125 kyr BP (Fig. 2) causing warmer summers than today in K125 by about 1 to 2 °C over Greenland (Fig. 4b). The final ice volume SLE value is in line with the various relative sea-level reconstructions displayed in Fig. 9a (red dot) and is also in agreement with the recent work by Stone et al. (2013) who estimate the contribution of the Greenland ice sheet during the last interglacial to be in the range 0.6 m–3.5 m SLE. The simulated final ice volume in SS236 is about −14.41 m SLE, which also fits the range of the various sea-level reconstructions [−35; −10] m SLE (Fig. 9b).

On the contrary, neither SS229 nor SS115 simulated final ice volumes match the range of observations. In SS229, the ice volume reaches −8.28 m SLE while observations indicate a global sea level of at least −50 m at that time. Similarly, in SS115, the simulated ice volume is −6.48 m SLE and the sea-level reconstructions indicate a sea level of at least −15 m SLE during that period. The discrepancies between our results and the sea-level reconstructions are, on one hand, due to the fact that in our climate simulations the only feedbacks acting at paleo-timescale are orbitals, greenhouse gases and the albedo of the sea-ice cover and, on the other hand, due to the uncertainties of the sea-level reconstructions themselves. Moreover, as explained in the previous section, the CESM shows a significant negative temperature bias in the high latitudes, which causes a substantial reduction in precipitation.

Since it is difficult to assess the direct impact of such bias in our paleo-ice-sheet simulations, we tested its importance on pre-industrial perennial snow and ice-sheet distribution. Simulated perennial snow cover in CTR1850 is limited to the Canadian archipelago, Svalbard and the islands of Barents Sea and Kara Sea (Fig. 7a). The high latitudes cold bias observed in CTR0k seems to not affect significantly pre-industrial perennial snow cover. What matters most is how the snow cover lasts during the summer. In the case of CTR1850, summer high latitudes insolation is larger by about 40 W m^{-2} relatively to K115 (Fig. 2a). In addition GHGs are larger in CTR1850 than in K115 (Table 1). Those differences causes a mean summer temperature warming of 3 °C in CTR1850 relatively to K115 over the northern high latitudes (Fig. 4a). This is enough to melt most of the winter snow over Eurasia and North America and prevent the accumulation of an extensive perennial snow cover.

To further investigate the impact in GRISLI, a 150 000 model-years steady-state experiment was performed using CTR1850 climatology and using the same parameters as for the paleo-experiments (Sect. 2.2.2). The ice-sheet distribution is in perfect agreement with the simulated perennial snow in CTR1850 (Fig. 7b). The final
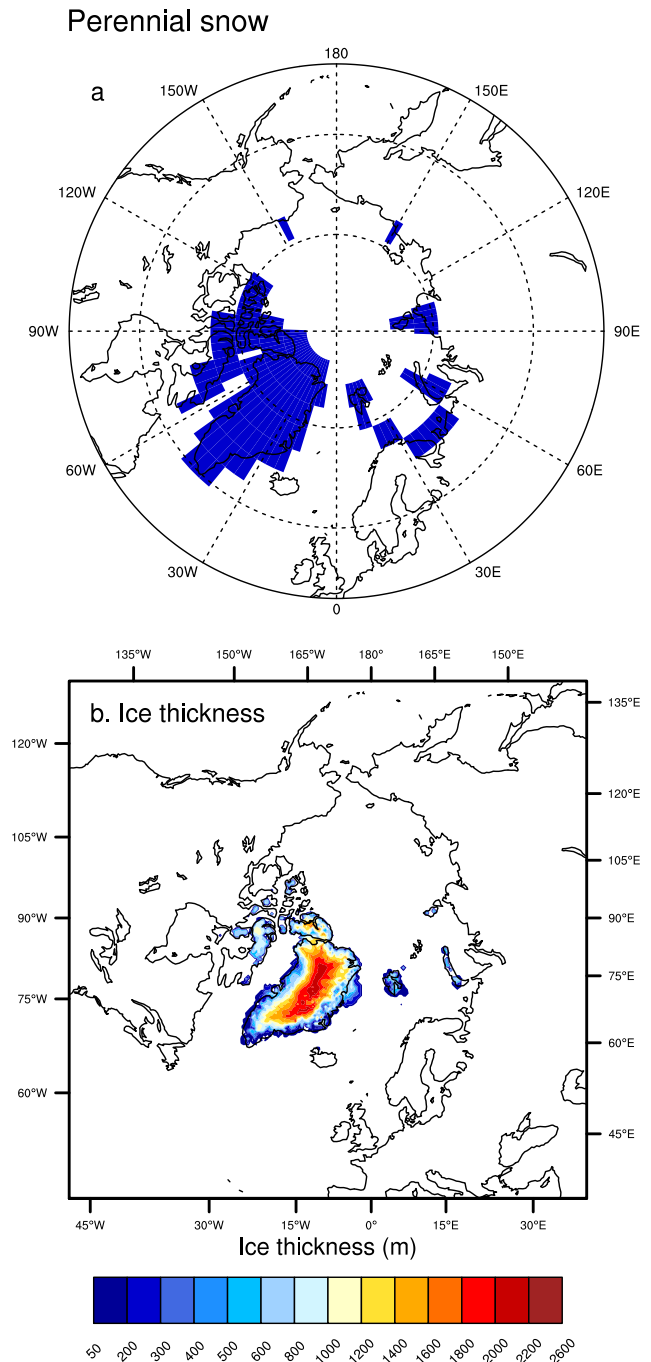
Perennial snow

Fig. 7. **(a)** Simulated perennial snow cover as in Fig. 5 from CTR1850 (Table 1). **(b)** Ice thickness (m) obtained after a 150 000 model year steady-state ice-sheet simulation using a mean annual lapse rate value of 5 °C km^{-1} and a summer lapse rate value of 4 °C km^{-1}.

ice volume is larger by about 1.7 m SLE relatively to initial ice volume (present-day Greenland ice sheet 7.1 m SLE). Most of accumulation occurs over the Canadian archipelago (≈ 1.2 m SLE). These results suggest that the cold temperature bias does not foster unrealistic and unreasonable
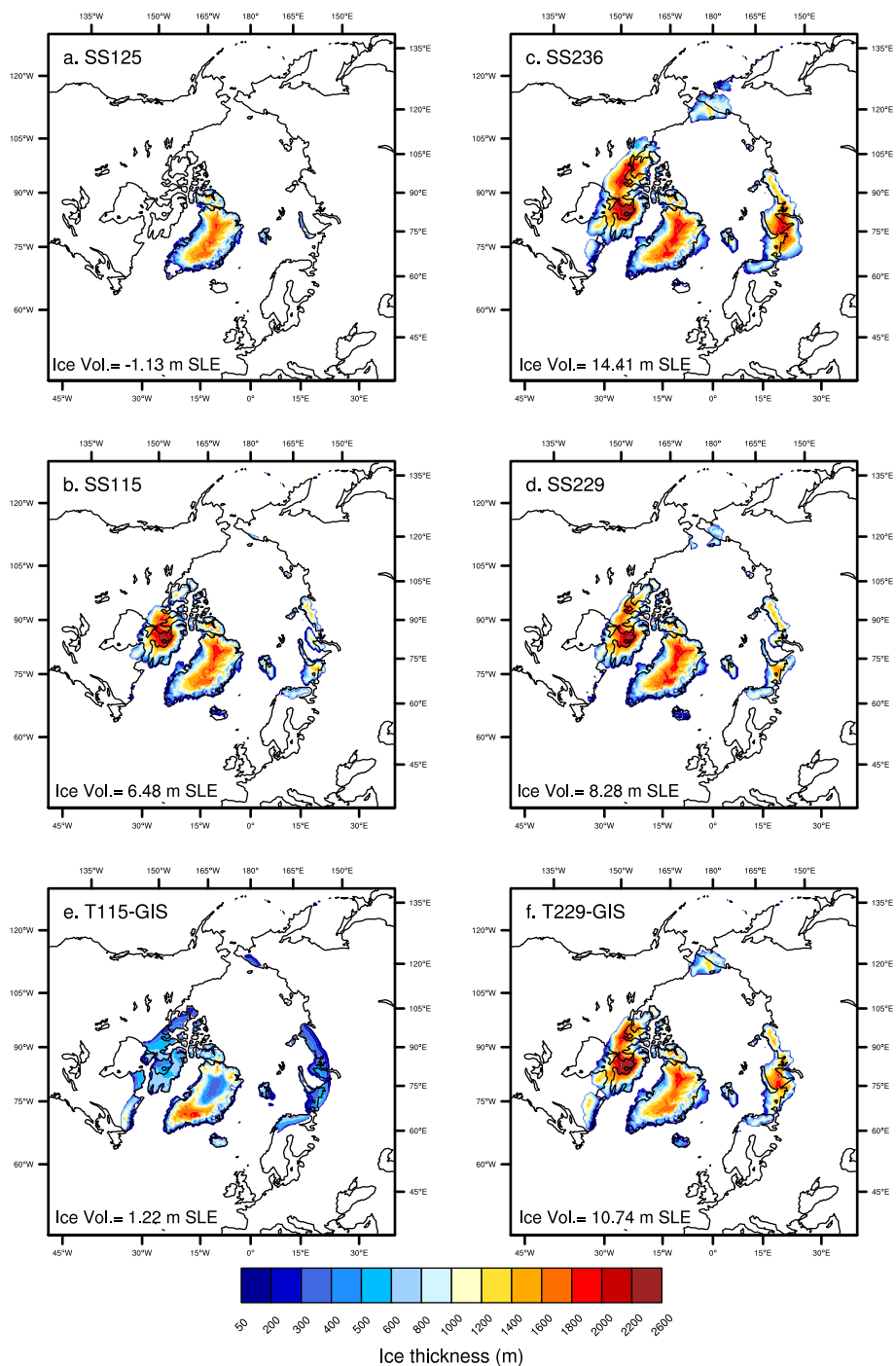
Fig. 8. Simulated ice thickness (m) for each of the steady-state experiments SS125 **(a)**, SS115 **(b)**, SS236 **(c)** and SS229 **(d)**. Simulated final ice thickness in meters for the transient experiments T115-GIS **(e)** and T229-GIS **(f)**. See Table 2 for details. Simulated total ice volume values for each experiment are expressed in meters sea-level equivalent (SLE) and are reported in each frame.

ice-sheet distribution over North America and Eurasia in GRISLI.

Since our climate simulations only account for orbitals, GHGs, and sea-ice albedo, how is it possible that SS125 and SS236 match the relative sea-level observations resulting

from the entire earth's climate system evolution and feedbacks? For SS125, the reason is linked to the orbital configuration of the period. Indeed, at 125 kyr BP, the summers are particularly warm and the reduced land-ice distribution induces a sea level higher than present day. This also implies
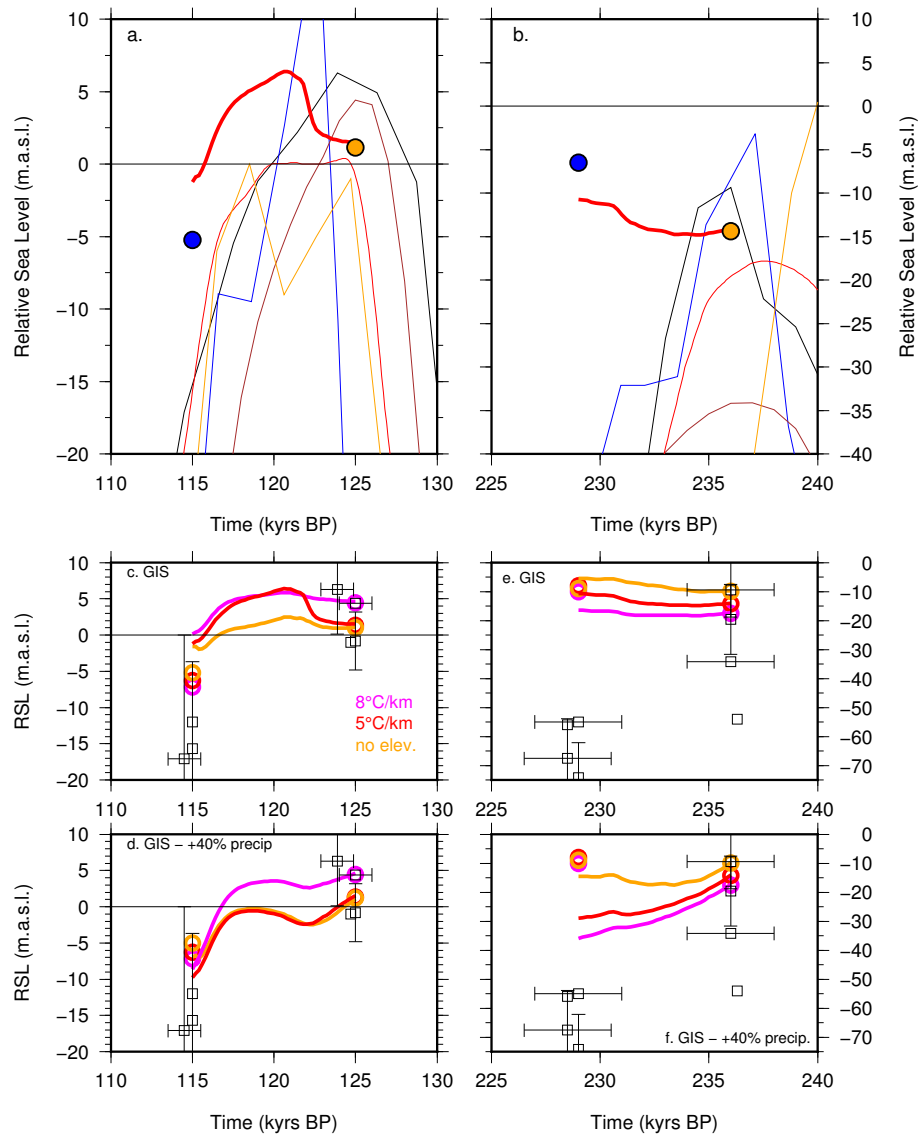
Fig. 9. Ice volume of steady-state experiments (blue and orange dots) and of transient experiments (thick red line) expressed in relative sea-level (m a.s.l.) for MIS 5 glacial inception period **(a)** and MIS 7 inception period **(b)**. Red thick line corresponds to transient experiments T115-GIS and T229-GIS ice volume evolution, forced using I_{GIS} index. Simulated values are compared to various paleo-sea-level observations: Waelbroeck et al. (2002) (black); Siddall et al. (2003) (blue); Shackleton (2000) (brown); Bintanja et al. (2005) (red) and Lea et al. (2002) (orange). Note that sea-level calculation does not account for ice volume developing over the Bering Strait and over the Himalaya areas as observed in our transient experiments (Fig. 8). Time evolution of ice volume of steady-state (empty circles) and transient (continuous and dotted line) experiments expressed in relative sea-level (m a.s.l.) for MIS 5 glacial inception period (**c** and **d**) and MIS 7 inception period (**e** and **f**). Each steady-state and transient experiment T115-GIS and T229-GIS was repeated three times according to different lapse rate values: $\lambda_0 = 0\,°C\,km^{-1}$ (orange) is the case not accounting for elevation changes, $\lambda_{5°C} = 5\,°C\,km^{-1}$ for annual temperature and $4\,°C\,km^{-1}$ for summer temperatures (red) and $\lambda_{8°C} = 8\,°C\,km^{-1}$ and $6.5\,°C\,km^{-1}$ (magenta). In frames **(d)** and **(f)**, precipitation was increased by 40 %. Simulated values are compared to various sea-level reconstructions (black empty squares) from Waelbroeck et al. (2002), Shackleton (2000), Bintanja et al. (2005) and Lea et al. (2002). No distinctions have been made between the reconstructions and error bars have been added when available.

that the land-ice albedo feedbacks are not significant compared to the other regional feedbacks and suggests that when we simulate climate at times where sea level is equal or higher than present day, the contributions of orbitals and GHGs to atmospheric temperature are enough to get a reasonable continental ice volume that fits with observations.

For SS236, when the orbital configuration places the precession at the end of October, the processes are similar. Part of the snow accumulated during the other seasons would melt

and the spatial extent of the perennial snow cover would be limited to the region where summer temperature is particularly cold (Figs. 4d and 5c). On the contrary, the perennial snow cover is as extensive as in K115 (Fig. 5d) and results from the particularly low level of GHGs which helps maintaining a negative air temperature in K236 (Table 1). Compared to K115, precipitation is larger over the inception areas than in K236, which is favorable to a more extended ice-sheet growth in SS236 than in SS115. This is why SS236 final ice volume reaches the upper bound of sea-level observations (Fig. 9b).

3.2.2 Transient ice-sheets experiments

The recent work of Köhler et al. (2010) aimed at calculating the individual contribution of the most important feedbacks acting on paleo-timescale to the mean annual global temperature signal: orbitals, GHGs, land-ice, sea-ice, vegetation and aeolian dust. They show that, during interglacials, the land-ice elevation and albedo feedbacks had a minor impact on the mean annual global temperature signal. On the contrary, they point out their increasing importance while climate cools until they become the most important contributions to the mean annual temperature signal approaching the glacial maxima. Similarly, with the steady-state experiments, we have shown that depending on the time period simulated, the lack of some of the regional feedbacks induces large discrepancies between simulated and observed/reconstructed past sea-level variations.

To further investigate this issue at those time periods, we performed two transient experiments. The temperature evolution between [K236; K229] and [K125; K115] is modulated by the index constructed after the works of Köhler et al. (2010) and Quiquet et al. (2013) (see Sect. 2.2.1). The I_{GIS} index (Eq. 3) is based on ΔT_{GIS} which corresponds to the combined impact of orbitals, GHGs and sea-ice-albedo feedbacks on air temperature (Eq. 2, Fig. 3d and e). These feedbacks are also included in our climate experiments K236, K229, K125 and K115 . . . Details are reported in Sect. 2 and in Table 2.

Ice-sheet distribution

The spatial distribution of the simulated final ice sheets for each of the transient experiments is shown in Fig. 8e and f. In T115-GIS, the final ice-sheet distribution is coherent with that obtained with the steady-state experiment SS115 (Fig. 8e). Ice sheets develop over the Canadian archipelago and south of the Baffin bay as well as over the Norwegian mountain range and the Eurasian Arctic islands (Fig. 8e). The ice over those areas is in general thinner than in SS115, because the I_{GIS} index substantially warms temperatures between 125 and 121 kyr BP (Fig. 10a and b) preventing ice sheets from accumulating over the inception areas and the accumulation over North America and Eurasia starts only

towards 120 kyr BP. The total accumulation time is then of about 5000 model years against 150 000 model years in the steady-state experiments. Consequently, the ice does not have time to thicken in T115-GIS as much as in SS115.

Similarly to T115-GIS, T229-GIS exhibits an ice-sheet distribution coherent with that obtained with the steady-state experiment SS229 (Fig. 8d and f). At odds with SS115 and T115-GIS, ice domes are thicker over Eurasia and North America in T229-GIS than in SS229. This happens because accumulation in SS229 is lower than in T229-GIS which benefits from the accumulation history since 236 kyr BP (Fig. 10f). Compared to T115-GIS, in T229-GIS ice-sheet dimensions do not vary much from their spin-up geometry because the climate contrast between K236 and K229 is smaller than between K125 and K115 (Fig. 4). Moreover, the use of I_{GIS}, whose values fluctuates around 1 (Fig. 3e), does not induce large additional climatic anomaly in T229-GIS (Fig. 10d and e).

The comparison between T115 and T229 experiments shows that the glacial inception at 229 kyr BP is more developed than at 115 kyr BP, since both North American and Eurasian ice sheets are thicker at 229 kyr BP, while it appears less obvious from the comparison between SS229 and SS115. The only unrealistic feature is the ice accumulation that occurs over the Bering Strait [. . .] in all the transient experiments (Fig. 8e and f). It has been shown that the existence of an ice sheet large enough over Eurasia could significantly affect the regional circulation by reducing the moisture advection that usually reaches eastern Siberian topographic highs, therefore stopping an ice cap from developing in this area (Krinner et al., 2011). However, the CESM simulations do not account for changes in topography caused by ice-sheet growth and the circulation patterns remain similar in eastern Siberia for all the simulations regardless of the period. Therefore, since there is no temperature or precipitation effect induced by a deviation in atmospheric circulation in our climate forcing, some ice develops over eastern Siberia in the transient ice experiments.

Comparison with sea-level reconstructions

The time evolution of the ice volume for each transient experiment is displayed in Fig. 9a and b. As expected, the ice volume evolution follows the main trends of the temperature index. In T115-GIS the ice volume first decreases until 121 kyr BP and then increases with cooling temperature (Fig. 9a). For T229-GIS, ice volume is stable until 231 kyr BP and slightly decreases until the end of the simulation because I_{GIS} induces a slight warming in temperature from this time (Fig. 10b and e).

Compared to sea-level observations, T115-GIS is not cold enough to enhance ice accumulation over the inception areas and to fit with observations (Fig. 9a). Nevertheless, T115-GIS final ice volume is much lower than in SS115 suggesting that the use of I_{GIS} does not decrease temperature
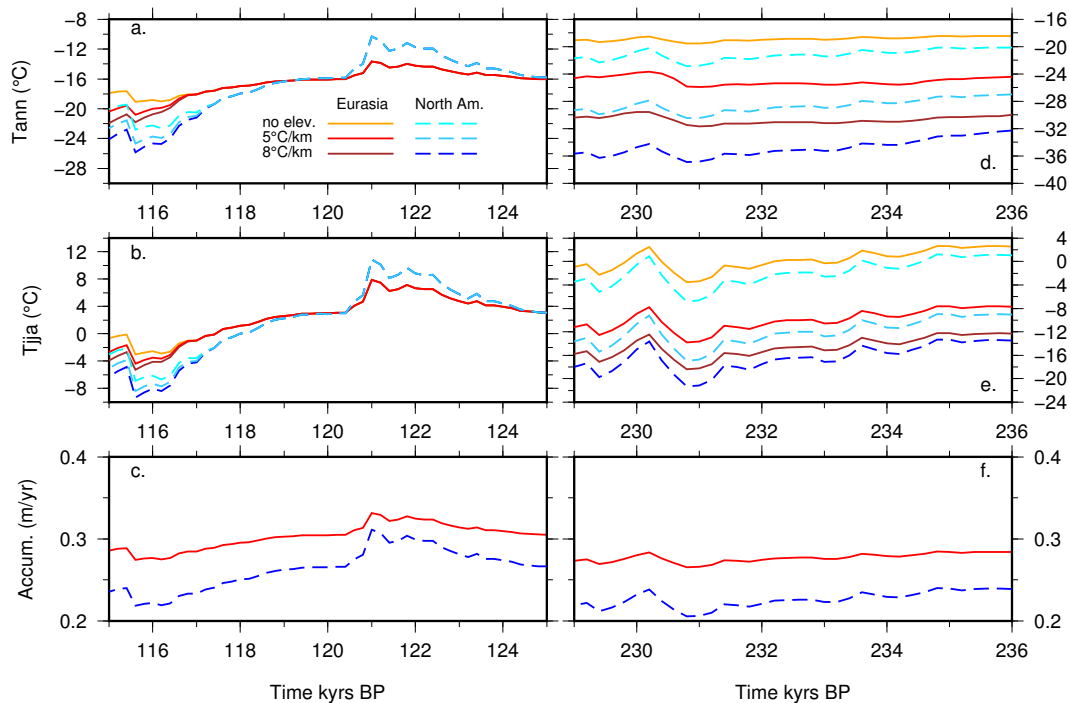
Fig. 10. Mean annual temperatures, July temperatures and mean annual precipitations time series resulting from Eqs. (5) and (6). Time series account for different lapse rates values: $\lambda_0 = 0\,°C\,km^{-1}$ is the case not accounting for elevation changes, $\lambda_{5°C} = 5\,°C\,km^{-1}$ for annual temperature and $4\,°C\,km^{-1}$ for summer temperatures and $\lambda_{8°C} = 8$ and $6.5\,°C\,km^{-1}$. Time series are displayed for MIS 5 (**a**, **b** and **c**) and for MIS 7 (**d**, **e** and **f**) time periods and show the climate evolution for Eurasia (red/orange colors) and North America (blue/cyan colors). Note that precipitation does not depend on the lapse rate, this is why there is only one time serie displayed for Eurasia (red), averaged over the Barents and Kara Seas, and North America (blue), averaged over the Hudson Bay and the Canadian archipelago.

enough to cause an increase in accumulation which compensates for the 150 000 model-year accumulation time of SS115 (blue dot). T229-GIS highly underestimates observations by more than 20 m SLE (Fig. 9b). The steady-state experiment SS236, together with sea-level reconstructions, suggests that some ice sheets probably already existed at this time period. In our climate simulation K236 we did not prescribe ice sheets over the inception areas. For that reason, simulated temperatures in K236 might be overestimated (i.e., too warm) compared to a climate simulation accounting for SS236 ice-sheet distribution as an initial condition. In addition, sea-level reconstructions suggest that ice sheets further developed until 229 kyr BP. The lack of prescribed ice sheets in climate simulation K229 also contributes to overestimate temperatures at this time, which is also supported by Quiquet et al. (2013) temperature index (Fig. 3c). The mismatch with paleo-observations is probably caused by a low accumulation resulting from the negative precipitation bias occurring over the inception areas in K229 climate forcing. This bias is further amplified by the precipitation scheme used in GRISLI (Eq. 6). The precipitation scheme follows the formulation of Greve (2005) which approximates the saturation vapor pressure in the atmosphere. In other words, this means that precipitation in GRISLI decreases with deceasing temperature,

and if temperatures are particularly cold, precipitation will be particularly low. The impact of precipitation bias, strengthened by the precipitation scheme of GRISLI, might strongly limit the ice accumulation in MIS 7 experiments.

3.2.3 Lapse rate and precipitation impact on ice-sheet distribution

The steady-state and transient experiments described in the previous sections account for a mean annual lapse rate of $5\,°C\,km^{-1}$ and a summer lapse rate of $4\,°C\,km^{-1}$ (hereafter, $\lambda_{5°C}$). To test the sensitivity of our simulations to lapse rate values, we performed two series of new steady-state and transient experiments similar to those described in Table 2 but (1) using a winter and summer lapse rates of 8 and $6.5\,°C\,km^{-1}$ (hereafter, $\lambda_{8°C}$) and (2) not accounting for elevation changes (both lapse rates set to 0, λ_0). Finally, all the transient experiments accounting for the three sets of lapse rate, $\lambda_{8°C}$, $\lambda_{5°C}$, λ_0, were run again increasing precipitation by 40 % homogeneously over the Northern Hemisphere. This last set of experiments was performed to test the sensitivity of our results to the precipitation bias observed in our coupled-model, high-latitude, present-day climate (Fig. 6c and d). In the following subsection, we focus our analysis on the impact
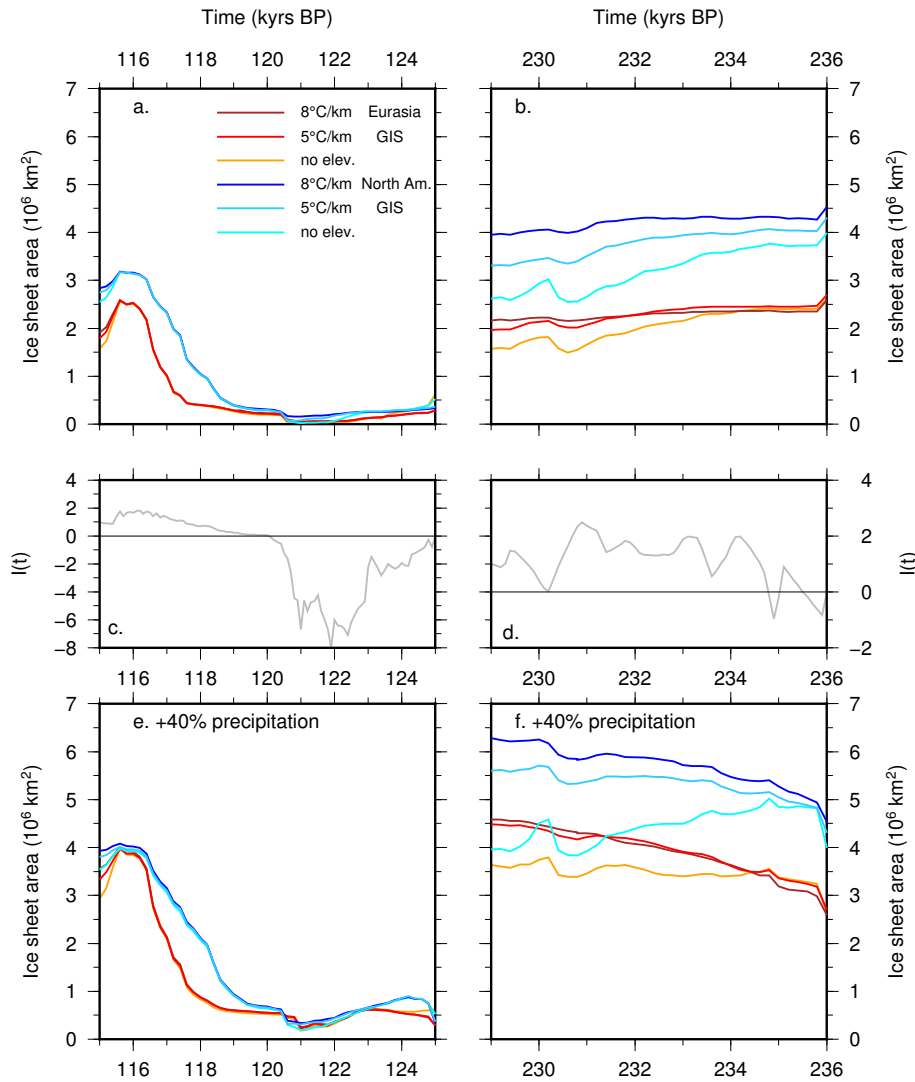
Fig. 11. Impact of lapse rate and precipitation formulation on ice-covered area of individual North American (blue colors) and Eurasian (red colors). Each transient experiment T115-GIS and T229-GIS was repeated three times according to different lapse rate values: $\lambda_0 = 0\,°C\,km^{-1}$ is the case not accounting for elevation changes, $\lambda_{5°C} = 5\,°C\,km^{-1}$ for annual temperature and $4\,°C\,km^{-1}$ for summer temperatures and $\lambda_{8°C} = 8$ and $6.5\,°C\,km^{-1}$. Results corresponding to Fig. 8c–d are plotted using red curves and in top frames. In frames **(a)** and **(b)**, precipitation formulation from Greve (2005) was used while in frames **(e)** and **(f)**, precipitation was increased by 40 %. In addition, in frames **(c)** and **(d)** I_{GIS} for both MIS 5 and MIS 7 time periods is displayed as in Fig. 3e and f.

of lapse rate and precipitation on the time evolution of ice volume (Fig. 9c–f) and ice area (Fig. 11).

For MIS 5 time period, the use of different lapse rates does not impact on the expansion rate of both ice sheets (Fig. 11a and e). The general shape of the curves is also well correlated to the shape of I_{GIS} (Fig. 11c). Note that ice starts expanding over North America and Eurasia only after 121 kyr BP because summer temperature is highly positive until this time causing a larger amount of ice melting (Fig. 10b). In addition, the North American ice sheet final area is larger than the Eurasian one (Fig. 11a) which suggests that in order to expand the Eurasian ice sheet, temperatures colder than those obtained using I_{GIS} are needed. In fact, mean annual

and summer temperatures over North America are lower than over Eurasia starting at 120–119 kyr BP (Fig. 10a and b).

When considering an overall increase of precipitation, final area over Eurasia has increased by 75 % and by about 45 % over North America (Fig. 11e). The Eurasian ice sheet is thus more sensitive to the lack of precipitation than the North American one, which might be related to the precipitation bias detected in CESM which is particularly strong over the Eurasian inception areas (Fig. 6c and d). However, increasing precipitation does not increase ice-sheet sensitivity to the various lapse rates (Fig. 11b).

In contrast with MIS 5 transient experiments, in the MIS 7 experiments, the use of different lapse rates induces

discrepancies in the ice areas over both North America and Eurasia: the largest ice area corresponds to the largest lapse rate value $\lambda_{8°C}$ (Fig. 11b and f). Both ice sheets are retreating (Fig. 11b) and the lower the λ, the larger the retreat. This behavior has a two fold explanation. First there is a reduction in precipitation caused by I_{GIS} along with a slight cooling of temperatures. Second, this cooling does not increase the area of possible ice accumulation contrary to what happens in T115-GIS (Fig. 10d–f). In contrast with T115-GIS experiments, increasing precipitation induces larger ice-sheet areas for both North America and Eurasia and enhances the differences obtained using the different lapse rates (Fig. 11f). Consequently, both ice sheets expand instead of retreating (Fig. 11f).

The impact of lapse rates is more important on MIS 5 ice volume than on MIS 5 ice area (Fig. 9c and d). First, steady-state experiments differ by about 5 m SLE between the largest lapse rate $\lambda_{8°C}$ and the case with no elevation changes accounted for λ_0 (Fig. 9c, circles). In addition, the various sets of transient experiments differ from 125 kyr BP to ≈ 119 kyr BP and the two $\lambda_{8°C}$ and $\lambda_{5°C}$ lapse rates contribute to the melting of more than half of the initial ice volume in SS125, while λ_0 only produces limited melting (Fig. 9c and d). After 119 kyr BP, no substantial difference is observed between the various lapse rates. This happens because temperature does not favor accumulation before 121 kyr BP (ΔT_{topo} in Eq. 5 equals 0). Nevertheless, in the T115-GIS experiments, increasing precipitation leads to a larger final ice volume, reaching the values of the steady-state experiments (Fig. 9d). This suggests that the larger precipitation compensates for the long accumulation time of SS115. However, while T115-GIS almost reaches the upper bound of paleo-observations, increasing precipitation together with prescribing a larger lapse rate value is not enough to generate a cooling which would allow ice volume to better match paleo-observations.

For MIS 7 experiments, the impact of the various lapse rates induces larger differences between the various steady-state simulations than in MIS 5 experiments (Fig. 9e). In fact, transient ice volume differs by 10 m SLE between the cases using λ_0 and the largest lapse rate value. This is twice as large as the difference generated by the different lapse rates in the transient experiments of MIS 5 time period. Contrary to what is obtained in T115-GIS, the lower bound of ice volume is given by the simulation discarding the elevation effect while the upper bound is given by $\lambda_{8°C}$ (Fig. 9e and f). This is due to the fact that temperature anomaly between 236 and 229 kyr BP always remains negative over inception areas and especially during summer while this is not the case between 125 and 115 kyr BP (Fig. 10). As a consequence, ice volume in T229-GIS simulations is always larger than present-day Northern Hemisphere ice volume. Similarly to T115-GIS, T229-GIS ice volumes do not fit with paleo-observations indicating that in this case, cooling alone is not enough to foster accumulation.

With larger precipitations, T229-GIS ice volumes still underestimate the observations by about 20 m SLE (Fig. 9e and f). The precipitation during MIS 7 is similar to MIS 5 over Eurasia but temperatures are much lower (Fig. 10). However, the final areas are almost the same for both time periods (Fig. 11e and f). which indicates that despite the cold temperatures, an increase of 40 % in precipitation is not enough to generate a larger ice volume and a larger ice area in the MIS 7 experiments that fit with paleo-observations. This suggests that for MIS 7 the lack of precipitation caused by the high-latitude temperature bias in CESM is mainly responsible for this discrepancy in ice volume.

4   Discussion

With two types of ice-sheet experiments, steady state and transient, we wanted to test the impact of external forcing (orbitals and GHGs) on the growth of ice sheets during the last two glacial inceptions. What we have shown in this work is that the steady-state ice distribution at both inception times differs from the transient one. The steady-state experiments (i.e., forced by steady-state simulated climates) underestimate the ice volume at both inceptions times (229 and 115 kyr BP), while the pre-inception simulated ice volumes (236 and 125 kyr BP) are in good agreement with observations. While increasing precipitations allows MIS 5 experiments to almost reach the upper bound of paleo-observations, for MIS 7, on the contrary, ice volume is underestimated, independently from the lapse rate value and the amount of precipitation. This suggests that the lack of precipitation detected in our CESM climate simulations, combined with the already cold MIS 7 climate induced by the external forcing over the inception areas stops the ice sheets from expanding and thickening at that time. Our conclusion is that cold biases are more effective during a cold inception, such as during MIS 7, than during a warm inception, such as MIS 5.

Coupled ice-sheet–climate simulations using fully coupled general circulation models spanning an entire glacial cycle are still constrained by available computational resources. An alternative to transient coupled simulations able to simulate time-varying ice distribution is the approach used in this work: simulate climatologies of the main climate tipping points, as glacial maxima and interglacials, and interpolate the climate in between by modulating temperature and/or precipitation by means of a time-varying index representative of those quantities. A nice example of this method is the work of Abe-Ouchi et al. (2007) who performed asynchronous simulations between an atmospheric GCM and an ISM to reconstruct the ice volume evolution during the entire last glacial cycle. They used the positive degree day mass balance scheme from Reeh (1991), as in GRISLI, and parametrized the input atmospheric surface temperature as the sum of the present-day climatology and the temperature anomalies, which are divided into terms due to ice-sheet

albedo feedback, CO_2, insolation feedback and a residual term (Köhler et al., 2010, followed a similar approach). In their dynamical ice-sheet model, accumulation is based on present-day observations which are modulated, through a power law, by the simulated surface temperature anomaly between two time periods. As in Charbit et al. (2002), the fact that this method is based on present-day climatology allows removal of climate model potential biases. As a result, Abe-Ouchi et al. (2007) were able to broadly reproduce a sea-level drop of about 130 m for the LGM (21 ky BP), using a lapse rate of $5\,°C\,km^{-1}$, in agreement with observations.

On the contrary, in our case, we deliberately use the simulated temperature and precipitation as reference climate to evaluate the capability of CESM with GRISLI to properly simulate different glacial inceptions. Furthermore, the fact that we use both steady-state and transient experiments allows us to highlight several important issues for both climate modeling and ice modeling. First of all, the steady-state ice experiments are very useful to understand the limits of climate forcing input in terms of temperature and precipitation. In all numerical models, a spin-up of the simulated variables is necessary, especially when thermodynamics is an active part of the simulated processes. However, in nature, the state of the earth's system at a given time depends on its evolution. This is particularly important for the components of the system that have long-term memory of climate changes, such as the deep ocean, the ice sheets and ice caps. Our results show that ISM steady-state experiments are efficient when the feedbacks accounted for into the climate simulations are likely to be the dominant feedbacks active during the epoch considered. In the case of our "interglacial" simulations at 125 and 236 kyr BP, orbitals, GHGs and the sea-ice albedo feedbacks are enough to simulate a reasonable steady-state ice distribution. On the other hand, both steady-state and transient experiments show that for the inception simulations at 115 and 229 kyr BP, those three feedbacks are not enough to give an ice volume which fits with the observations. The combination of steady-state and transient ice experiments is highly powerful in our case to evidence the limits and biases of our models combination.

As we showed, our present-day anthropogenic climate simulation (CTR0k) presents strong winter negative temperature bias over the Eurasian inception areas causing a reduction in precipitation. If we assume that the cold bias was likely propagated into our past climate simulations, it could have affected the inception process in GRISLI (i) by enhancing the glacial inception, as previously shown in Vettoretti and Peltier (2003), and/or (ii) by resulting in a significant reduction in precipitation over the Eurasian Arctic regions. However, our transient simulations show that those biases do not have the same importance during MIS 5 and MIS 7 and that their contribution depends on the mean background climate state of the epoch considered. Indeed, in our "warm" glacial inception (MIS 5), the high summer temperature at 125 kyr BP inhibits the growth of ice sheets despite the

negative temperature bias in the high latitudes, because at that time it is the impact of precession on high latitude climate that mostly matters. On the other hand, in our "cold" glacial inception (MIS 7) the summer temperature is particularly low, due to the low level of GHGs, and causes the climate to be particularly dry. In this case, the dryness strengthens the negative precipitation bias by limiting the amount of ice accumulating over the high latitudes.

To improve those results, an alternative approach could be to apply a correction on precipitation and/or temperatures over the regions affected by the biases. Some previous studies using coupled ice-sheet–climate models tested the implementation of "patches" for precipitation over the areas of inceptions to counteract the climate model bias (e.g., Bonelli et al., 2009; Ganopolski et al., 2010). However, applying patches over some particular areas greatly limits the validation of the capability of coupled systems to reproduce glacial inceptions where the geological evidence indicate the presence of past ice sheets. It unnaturally forces the response of the climate and ice-sheet models. Moreover, it also limits investigations of whether coupled systems are able to reproduce different spatial ice-sheet distributions during older glacial cycles. This solution might be applied only if the aim of the numerical experiments is beyond the scope of validating and calibrating the models to improve the simulation of climate processes.

A last caveat concerns the resolution of the CESM simulations. Compared to Jochum et al. (2011), we simulated the same glacial inception ($\approx 115\,kyr\,BP$) starting from a colder mean ocean state spin-up (here 125 kyr BP) and with a coarser horizontal resolution (T31). As a result, the simulated perennial snow cover seems to be slightly less extensive at lower resolution, implying that resolution is important for the simulation of polar processes as suggested in the previous work of Vavrus et al. (2011). Simulating the climate at a higher spatial resolution would likely improve the glacial inception in the climate models, especially over high topographies where numerous GCMs usually fail to calculate correct precipitation patterns (Bonelli et al., 2009). It would also contribute to resolve the melting processes along the margins of the ice sheets, which are critical for the advance and/or retreat of the ice sheets over continental areas laying below a certain latitude (e.g., Colleoni et al., 2009b).

In literature, some of the numerous climate modeling studies focusing on the last glacial inception (see references in Sect. 1) conclude that they succeed in reproducing glacial inception only by looking at the extent and amount of perennial snow cover on the Northern Hemisphere high latitudes. If we follow a paleo-data approach, nucleation sites for the first ice dynamics are classically the Canadian archipelago, the Cascades and the Rocky mountains, the Svalbard and the islands in Barents Sea and Kara Sea. Based on this evidence, it becomes difficult to assess whether a climate model can accurately reproduce glacial inceptions without using a dynamical ISM to define the areas where ice dynamics

effectively took place in the past. Results in Charbit et al. (2007) show that the spatial distribution of the simulated ice cover is highly model dependent. In some experiments the extent of ice cover matches that of the perennial snow cover of the GCMs, while in others it remains limited to some of the Arctic islands.

It is tempting to say that ice experiments leading to the growth of an ice sheet wherever the snow is perennial in GCMs, even in areas in which geological evidence suggests as "ice free", hold a bias inherited from the climate model. The persistence of mismatch between the ice cover in the ISM and the perennial snow cover in the GCMs shows the necessity of better understanding the physics and the schemes embedded in our climate and ice-sheet models in order to perform reliable simulations in various climate contexts. However, the limits of the method used in Charbit et al. (2007), Abe-Ouchi et al. (2007), as well as in our present study, are the absence of direct elevation and albedo feedbacks between atmosphere and ice sheets. These feedbacks are important for the ice sheet's growth and for their effect on the synoptic circulation (e.g., Kageyama et al., 2004; Liakka and Nilsson, 2010; Herrington and Poulsen, 2012). However, as we show with our transient experiments, the impact of precipitation bias is more important than the effect of atmospheric lapse rate.

The recent work of Gregory et al. (2012) is one of the first attempt to couple an ice-sheet model to an AOGCM. Although the coupled simulations of the last glacial inception are successful, the ice-sheet model used in Gregory et al. (2012) does not account for ice-shelf dynamics contrary to GRISLI. "As a consequence, in our experiments, the ice sheets are able to flow over the marine domain, in between the small islands of the Barent Sea and over the Hudson bay, which represent nucleation sites for the growth of ice sheets. Those processes are important for the whole dynamics of the ice sheets and give more emphasis to the inception." On the continental domain, our results are similar to those of Gregory et al. (2012) over North America but differ over Norway (in Gregory et al., 2012, the Eurasian grid is restricted to western Europe and does not allow for a full comparison with our results. Furthermore, the discrepancies can also result from the climate bias over Eurasia in our CESM simulations). This suggests that the climate–ice-sheet feedbacks are more important for ice accumulation over western Europe than over North America, highlighting the necessity to proceed with coupled climate–ice-sheet simulations.

5 Conclusions

The present manuscript aimed at comparing the last two glacial inceptions that we defined as "warm" glacial inception and "cold" glacial inception accordingly to the initial state of the ice distribution over continents. The results show that external forcing factors dominate the Northern Hemisphere high-latitudes climate during interglacials while without proper ice-elevation and albedo feedbacks, external forcing alone cannot simulate the evolution towards glacial inception, especially for the MIS 5 time period. Nevertheless, our simulations also show that depending on the mean background climate state, the effect of climate model biases can have different consequences on the growth of ice sheets at those periods. Although the precipitation bias always affects the inception processes in GRISLI, glacial inception during MIS 5 can be simulated more easily than during MIS 7. Indeed an increased precipitation applied to compensate the bias, combined with glacial-friendly external forcing, is enough to produce an ice volume that fits sea-level observations. In addition, MIS 5 ISM experiments have shown to be more sensitive to precipitation changes than to changes in prescribed lapse rate values.

On the contrary, MIS 7 ISM experiments are sensitive to both lapse rate variations and precipitation changes because both MIS 7 simulated climates are colder than MIS 5 simulated climates as a result of external forcing. However, MIS 7 ice sheets always underestimate observations, even accounting for a substantial increase in precipitation. This suggests that CESM temperature and precipitation biases have a larger effect on the colder climates (MIS 7) than on warmer climates (MIS 5). Furthermore, it also suggests that to simulate MIS 7 properly, coupled models are necessary to account for the land-ice albedo feedback. There is indeed evidence from sea-level reconstructions showing that during MIS 7, some ice sheets survived to the previous glacial cycle and the land-ice albedo feedback might be essential to increase the ice volume. However, also including the land-ice albedo feedback, it might not be enough to solve the problems of the impact of systematic GCMs biases on ISM surface mass balance.

Our results confirm that glacial inceptions are particularly interesting because they represent transient states between warmer to colder climates (Calov et al., 2005b), when the Northern Hemisphere synoptic circulation is not yet too much affected by changes in topography and the amplitude of the temperature anomaly is not as large as during glacial maxima. They constitute an interesting test for the new generation of earth system models.

Edited by: U. Mikolajewicz

References

Abe-Ouchi, A., Segawa, T., and Saito, F.: Climatic Conditions for modelling the Northern Hemisphere ice sheets throughout the ice age cycle, Clim. Past, 3, 423–438, doi:10.5194/cp-3-423-2007, 2007.

Adler, R., Huffman, G., Chang, A., Ferraro, R., Xie, P., Janowiak, J., Rudolf, B., Schneider, U., Curtis, S., Bolvin, D., Gruber, A., Susskind, J., and Arkin, P.: The Version 2 Global Precipitation Climatology Project (GPCP) Monthly Precipitation Analysis (1979–Present), J. Hydrometeorol., 4, 1147–1167, 2003.

Álvarez-Solas, J., Montoya, M., Ritz, C., Ramstein, G., Charbit, S., Dumas, C., Nisancioglu, K., Dokken, T., and Ganopolski, A.: Heinrich event 1: an example of dynamical ice-sheet reaction to oceanic changes, Clim. Past, 7, 1297–1306, doi:10.5194/cp-7-1297-2011, 2011.

Berger, A. L.: Long-term variations of daily insolation and quaternary climatic changes, J. Atmos. Sci., 35, 2362–2367, 1978.

Bintanja, R., van de Wal, R. S., and Oerlemans, J.: Modelled atmospheric temperatures and global sea levels over the past million years, Nature, 437, 126–128, 2005.

Bonelli, S., Charbit, S., Kageyama, M., Woillez, M.-N., Ramstein, G., Dumas, C., and Quiquet, A.: Investigating the evolution of major Northern Hemisphere ice sheets during the last glacial-interglacial cycle, Clim. Past, 5, 329–345, doi:10.5194/cp-5-329-2009, 2009.

Born, A., Kageyama, M., and Nisancioglu, K. H.: Warm Nordic Seas delayed glacial inception in Scandinavia, Clim. Past, 6, 817–826, doi:10.5194/cp-6-817-2010, 2010.

Calov, R. and Marsiat, I.: Simulations of the Northern Hemisphere through the last glacial-interglacial cycle with a vertically integrated and a three-dimensional thermomechanical ice sheet model coupled to a climate model, Ann. Glaciol., 27, 169–176, 1998.

Calov, R., Ganopolsi, A., Petoukhov, V., Claussen, M., Brovkin, V., and Kutbatzki, C.: Transient simulation of the last glacial inception, Part II: sensitivity and feedback analysis, Clim. Dynam., 24, 563–576, 2005a.

Calov, R., Ganopolski, A., Claussen, M., Petoukhov, V., and Greve, R.: Transient simulation of the last glacial inception, Part I: glacial inception as a bifurcation in the climate system, Clim. Dynam., 24, 545–561, 2005b.

Caputo, R.: Sea-level curves: perplexities of an end-user in morphotectonic applications, Global Planet. Change, 57, 417–423, 2007.

Charbit, S., Ritz, C., and Ramstein, G.: Simulations of Northern Hemisphere ice-sheet retreat: sensitivity to physical mechanisms involved during the Last Deglaciation, Quaternary Sci. Rev., 21, 245–263, 2002.

Charbit, S., Ritz, C., Philippon, G., Peyaud, V., and Kageyama, M.: Numerical reconstructions of the Northern Hemisphere ice sheets through the last glacial-interglacial cycle, Clim. Past, 3, 15–37, doi:10.5194/cp-3-15-2007, 2007.

Colleoni, F., Krinner, G., and Jakobsson, M.: Sensitivity of the Late Saalian (140 kyrs BP) and LGM (21 kyrs BP) Eurasian ice sheet surface mass balance to vegetation feedbacks, Geophys. Res. Lett., 36, L08704, doi:10.1029/2009GL037200, 2009a.

Colleoni, F., Krinner, G., Jakobsson, M., Peyaud, V., and Ritz, C.: Influence of regional factors on the surface mass balance of the large Eurasian ice sheet during the peak Saalian (140 kyrs BP), Global Planet. Change, 68, 132–148, 2009b.

de Noblet, N., Prentice, I. C., Jousseaume, S., Texier, D., Botta, A., and Haxeltine, A.: Possible role of atmosphere-biosphere interactions in triggering the last deglaciation, Geophys. Res. Lett., 23, 3191–3194, 1996.

Dong, B. and Valdes, P.: Sensitivity studies of Northern Hemisphere glaciation using an atmospheric general circulation model, J. Climate, 8, 2471–2496, 1995.

Dutton, A., Bard, E., Antonioli, F., Esat, T., Lambeck, K., and McCulloch, M.: Phasing and amplitude of sea-level and climate change during the penultimate interglacial, Nat. Geosci., 2, 355–359, 2009.

Ganopolski, A. and Calov, R.: Simulation of glacial cycles with an Earth system model, in: Climate Change, Springer, Vienna, 49–55, 2012.

Ganopolski, A., Calov, R., and Claussen, M.: Simulation of the last glacial cycle with a coupled climate ice-sheet model of intermediate complexity, Clim. Past, 6, 229–244, doi:10.5194/cp-6-229-2010, 2010.

Gent, P. R., Danabasoglu, G., Donner, L. J., Holland, M. M., Hunke, E. C., Jayne, S. R., Lawrence, D. M., Neale, R. B., Rasch, P. J., Vertenstein, M., Worley, P. H., Yang, Z.-L., and Zhang, M.: The Community Climate System Model Version 4, J. Climate, 24, 4973–4991, 2011.

Gregory, J. M., Browne, O. J. H., Payne, A. J., Ridley, J. K., and Rutt, I. C.: Modelling large-scale ice-sheet–climate interactions following glacial inception, Clim. Past, 8, 1565–1580, doi:10.5194/cp-8-1565-2012, 2012.

Greve, R.: Relation of measured basal temperatures and the spatial distribution of the geothermal heat flux for the Greenland ice sheet, Ann. Glaciol., 42, 424–432, 2005.

Herrington, A. R. and Poulsen, C. J.: Terminating the Last Interglacial: The Role of Ice Sheet-Climate Feedbacks in a GCM Asynchronously Coupled to an Ice Sheet Model, J. Climate, 25, 1871–1882, 2012.

Hutter, K.: Theoretical glaciology: material science of ice and the mechanics of glaciers and ice sheets, Reidel Publishing Company, Dordrecht, the Netherlands, 1983.

Jackson, C. and Broccoli, A.: Orbital forcing of Arctic climate: mechanisms of climate response and implications for continental glaciation, Clim. Dynam., 21, 539–557, 2003.

Jochum, M., Jahn, A., Peacock, S., Bailey, D., Fasullo, J., Kay, J., Levis, S., and Otto-Bliesner, B.: True to Milankovitch: Glacial Inception in the new Community Climate System Model, J. Climate, 25, 2226–2239, doi:10.1175/JCLI-D-11-00044.1, 2011.

Jouzel, J., Masson-Delmotte, V., Cattani, O., Dreyfus, G., Falourd, S., Hoffmann, G., Minster, B., Nouet, J., Barnola, J., Chappellaz, J., Fischer, H., Gallet, J., Johnsen, S., Leuenberger, M., Loulergue, L., Luethi, D., Oerter, H., Parrenin, F., Raisbeck, G., Raynaud, D., Schilt, A., Schwander, J., Selmo, E., Souchez, R., Spahni, R., Stauffer, B., Steffensen, J., Stenni, B., Stocker, T., Tison, J., Werner, M., and Wolff, E.: Orbital and Millennial Antarctic Climate Variability over the Past 800,000 Years, Science, 317, 793–797, 2007.

Kageyama, M., Charbit, S., Ritz, C., Khodri, M., and Ramstein, G.: Quantifying ice-sheet feedbacks during the last glacial inception, Geophys. Res. Lett., 31, L24203, doi:10.1029/2004GL021339, 2004.

Kalnay, E., Kanamitsu, M., Kistler, R., Collins, W., Deaven, D., Gandin, L., Iredell, M., Saha, S., White, G., Woollen, J., Zhu, Y., Chelliah, M., Ebisuzaki, W., Higgins, W., Janowiak, J., Mo, K. C., Ropelewski, C., Wang, J., Leetmaa, A., Reynolds, R., Jenne, R., and Joseph, D.: The NCEP/NCAR 40-year reanalysis project, B. Am. Meteorol. Soc., 77, 437–470, 1996.

Khodri, M., Leclainche, Y., Ramstein, G., Braconnot, P., Marti, O., and Cortijo, E.: Simulating the amplification of orbital forcing by ocean feedbacks in the last glaciation, Nature, 410, 570–574, 2001.

Kirchner, N., Greve, R., Stroeven, A. P., and Heyman, J.: Paleoglaciological reconstructions for the Tibetan Plateau during the last glacial cycle: evaluating numerical ice sheet simulations driven by GCM-ensembles, Quaternary Sci. Rev., 30, 248–267, 2011.

Köhler, P., Bintanja, R., Fischer, H., Joos, F., Knutti, R., Lohmann, G., and Masson-Delmotte, V.: What caused Earth's temperature variations during the last 800,000 years? Data-based evidences on radiative forcing and constraints on climate sensitivity, Quaternary Sci. Rev., 29, 129–145, 2010.

Kopp, R. E., Simons, F. J., Mitrovica, J. X., Maloof, A. C., and Oppenheimer, M.: Probabilistic assessment of sea level during the last interglacial stage, Nature, 462, 863–868, 2009.

Krinner, G., Boucher, O., and Balanski, Y.: Ice-free glacial northern Asia due to dust deposition on snow, Clim. Dynam., 27, 773–777, 2006.

Krinner, G., Diekmann, B., Colleoni, F., and Stauch, G.: Global, regional and local scale factors determining glaciation extent in Eastern Siberia over the last 140,000 years, Quaternary Sci. Rev., 30, 821–831, 2011.

Kubatzki, C., Claussen, M., Calov, R., and Ganopolski, A.: Sensitivity of the last glacial inception to initial and surface conditions, Clim. Dynam., 27, 333–344, 2006.

Laskar, J., Robutel, P., Joutel, F., Gastineau, M., Correia, A. C. M., and Levrard, B.: A long-term numerical solution for the insolation quantities of the Earth, Astron. Astrophys., 428, 261–285, 2004.

Lea, D. W., Martin, P. A., Pak, D. K., and Spero, H. J.: Reconstructing a 350 ky history of sealevel using planktonic Mg/Ca and oxygen isotope records from a Cocos Ridge core, Quaternary Sci. Rev., 21, 283–293, 2002.

Letréguilly, A., Reeh, N., and Huybrechts, P.: The Greenland ice sheet through the last glacial-interglacial cycle, Global Planet. Change, 4, 385–394, 1991.

Liakka, J. and Nilsson, J.: The impact of topographically forced stationary waves on local ice-sheet climate, J. Glaciol., 56, 534–544, 2010.

Loulergue, L., Schilt, A., Spahni, R., Masson-Delmotte, V., Blunier, T., Lemieux, B., Barnola, J.-M., Raynaud, D., Stocker, T., and Chappellaz, J.: Orbital and millennial-scale features of atmospheric CH_4 over the past 800,000 years, Nature, 453, 383–386, 2008.

Luthi, D., Floch, M. L., Bereiter, B., Blunier, T., Barnola, J.-M., Siegenthaler, U., Raynaud, D., Jouzel, J., Fischer, H., Kawamura, K., and Stocker., T.: High-resolution carbon dioxide concentration record 650,000–800,000 years before present, Nature, 453, 379–382, 2008.

MacAyeal, D.: Large-Scale Ice Flow Over a Viscous Basal Sediment: Theory and Application to Ice Stream B, Antarctica, J. Geophys. Res., 94, 4071–4087, 1989.

Martrat, B., Grimalt, J. O., Shackleton, N. J., de Abreu, L., Hutterli, M. A., and Stocker, T. F.: Destabilizations on the Iberian Margin Four Climate Cycles of Recurring Deep and Surface Water, Science, 317, 502–507, 2007.

Masson-Delmotte, V., Stenni, B., Pol, K., Braconnot, P., Cattani, O., Falourd, S., Kageyama, M., Jouzel, J., Landais, A., Minster, B., Krinner, G., Johnsen, S., Röthlisberger, R., Chappellaz, J., Hansen, J., Mikolajewicz, U., and Otto-Bliesner, B.: EPICA Dome C record of glacial and interglacial intensities, Quaternary Sci. Rev., 29, 113–128, 2010.

McCulloch, M. T. and Esat, T.: The coral record of last interglacial sea levels and sea surface temperatures, Chem. Geol., 169, 107–129, 2000.

Meissner, K., Weaver, A., Matthews, H., and Cox, P.: The role of land surface dynamics in glacial inception: a study with the UVic Earth system model, Clim. Dynam., 21, 515–537, 2003.

North GRIP members: High-resolution record of northern hemisphere climate extending into the last interglacial period, Nature, 431, 147–151, 2004.

Oppo, D. W., McManus, J. F., and Cullen, J. L.: Evolution and demise of the last interglacial warmth in the subpolar North Atlantic, Quaternary Sci. Rev., 25, 3268–3277, 2006.

Peyaud, V., Ritz, C., and Krinner, G.: Modelling the Early Weichselian Eurasian Ice Sheets: role of ice shelves and influence of ice-dammed lakes, Clim. Past, 3, 375–386, doi:10.5194/cp-3-375-2007, 2007.

Quiquet, A.: Reconstruction de la calotte polaire du Groenland au cours du dernier cycle glaciaire-interglaciaire à partir de l'association de la modélisation numérique 3D et des enregistrements des carottages glaciaires profonds, Ph.D. thesis, Université Grenoble I, LGGE, Grenoble, 2012.

Quiquet, A., Ritz, C., Punge, H. J., and Salas y Mélia, D.: Greenland ice sheet contribution to sea level rise during the last interglacial period: a modelling study driven and constrained by ice core data, Clim. Past, 9, 353–366, doi:10.5194/cp-9-353-2013, 2013.

Rabineau, M., Berne, S., Olivet, J., Aslanian, D., Guillocheau, F., and Joseph, P.: Paleo sea levels reconsidered from direct observation of paleoshore-line position during glacial maxima (for the last 500,000 yr), Earth Planet. Sc. Lett., 252, 119–137, 2006.

Reeh, N.: Parameterization of Melt Rate and Surface Temperature on the Greenland Ice Sheet, Polarforschung, 5913, 113–128, 1991.

Rind, D., Peteet, D., and Kukla, G.: Can Milankovitch orbital variations initiate the growth of ice sheets in a general circulation model?, J. Geophys. Res., 94, 12851–12871, 1989.

Ritz, C., Rommalaere, V., and Dumas, C.: Modeling the evolution of Antarctic ice sheet over the last 420,000 years: Implications for altitude changes in the Vostok region, J. Geophys. Res., 106, 31943–31964, 2001.

Rommelaere, V. and Ritz, C.: A thermomechanical model of ice-shelf flow, Ann. Glaciol., 23, 13–20, 1996.

Schilt, A., Baumgartner, M., Blunier, T., Schwander, J., Spahni, R., Fischer, H., and Stocker, T.: Glacial-Interglacial and Millennial Scale Variations in the Atmospheric Nitrous Oxide Concentration during the last 800,000 Years, Quaternary Sci. Rev., 29, 182–192, 2010.

Shackleton, N.: The 100,000-Year Ice-Age Cycle Identified and Found to Lag Temperature, Carbon Dioxide, and Orbital Eccentricity, Science, 289, 1897–1902, 2000.

Shapiro, N. and Ritzwoller, M.: Inferring surface heat flux distributions guided by a global seismic model: particular ap- plication to Antarctica, Earth Planet. Sc. Lett., 223, 213–214, 2004.

Shields, C., Bailey, D., Danabasoglu, G., Jochum, M., Kiehl, J., Levis, S., and Park, S.: The Low Resolution CCSM4, J. Climate, 25, 3993–4014, 2012.

Siddall, M., Rohling, E. J., Almogi-Labin, A., Hemleben, C., Meischner, D., Schmelzer, I., and Smeed, D. A.: Sea-level fluctuations during the last glacial cycle, Nature, 423, 853–858, 2003.

Stirling, C. H., Esat, T., McCulloch, M. T., and Lambeck, K.: High-precision U-series dating of corals from Western Australia and implications for the timing and duration of the Last Interglacial, Earth Planet. Sc. Lett., 135, 115–130, 1995.

Stone, E. J., Lunt, D. J., Annan, J. D., and Hargreaves, J. C.: Quantification of the Greenland ice sheet contribution to Last Interglacial sea level rise, Clim. Past, 9, 621–639, doi:10.5194/cp-9-621-2013, 2013.

Vavrus, S., Philippon-Berthier, G., Kutzbach, J. E., and Ruddiman, W. F.: The role of GCM resolution in simulating glacial inception, Holocene, 21, 819–830, 2011.

Vettoretti, G. and Peltier, W. R.: Post-Eemian Glacial Inception, Part I: The Impact of Summer Seasonal Temperature Bias, J. Climate, 16, 889–911, 2003.

Vettoretti, G. and Peltier, W.: Sensitivity of glacial inception to orbital and greenhouse gas climate forcing, Quaternary Sci. Rev., 23, 499–519, 2004.

Waelbroeck, C., Labeyrie, L., Michel, E., Duplessy, J., McManus, J., Lambeck, K., Balbon, E., and Labracherie, M.: Sea-level and deep water temperature changes derived from benthic foraminifera isotopic records, Quaternary Sci. Rev., 21, 295–305, 2002.

Wang, Z. and Mysak, L.: Simulation of the last glacial inception and rapid ice sheet growth in the McGill Paleoclimate Model, Geophys. Res. Lett., 29, 17-1–17-4, 2002.

Yoshimori, M., Reader, M., Weaver, A., and McFarlane, N.: On the causes of glacial inception at 116 ka BP, Clim. Dynam., 18, 383–402, 2002.